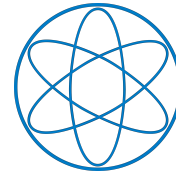




Fakultät für Elektrotechnik  
und Informationstechnik



TECHNISCHE  
UNIVERSITÄT  
MÜNCHEN

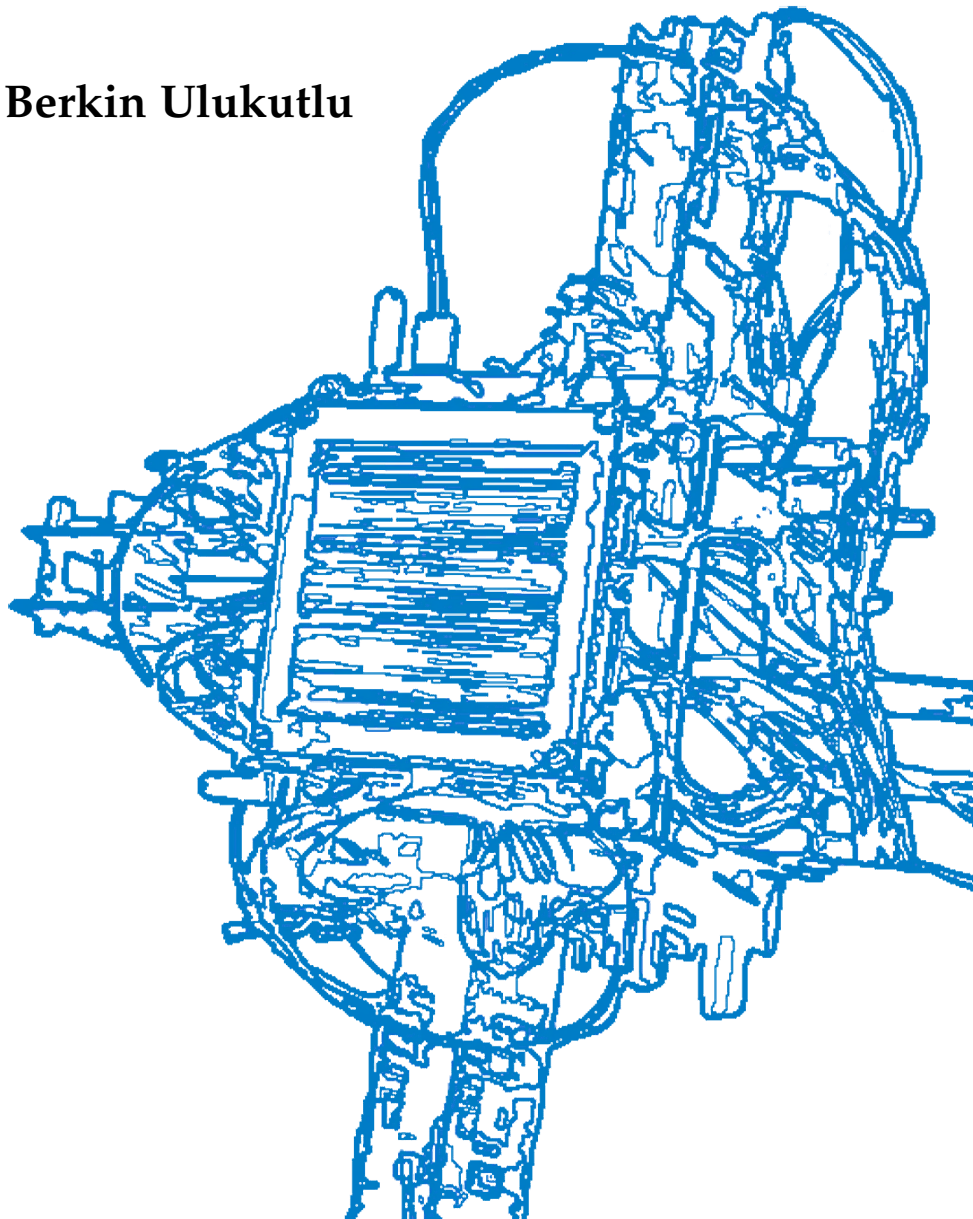


Fakultät für Physik

Master's Thesis

# A search for new materials and the development of a readout system for particle detector applications

Berkin Ulukutlu





TECHNISCHE UNIVERSITÄT MÜNCHEN



Fakultät für Elektrotechnik  
und Informationstechnik



Fakultät für Physik

# **A search for new materials and the development of a readout system for particle detector applications**

## **Untersuchung neuer Materialien und die Entwicklung eines Auslesesystems für Teilchendetektoranwendungen**

Master's Thesis

**Author:** Berkin Ulukutlu  
**Examiner:** Prof. Dr. Reinhard Kienberger  
**Supervisor:** Prof. Dr. Laura Fabbietti  
**Advisor:** Dr. Piotr Gasik  
**Date:** 18.10.2021

I confirm that the results presented in this master's thesis is my own work and I have documented all sources and materials used.

Ich versichere, dass ich diese Masterarbeit selbstständig verfasst und nur die angegebenen Quellen und Hilfsmittel verwendet habe.

Munich, 18.10.2021

Berkin Ulukutlu

# Abstract

Improving existing particle detector designs and developing new detection technologies is crucial for the advancement of the scientific frontier. The presented thesis covers two projects investigating different particle detector designs. Firstly, Gas Electron Multipliers (GEM), a Micro-Pattern-Gas-Detector commonly utilized in major particle physics experiments are studied. GEMs are limited in their long-term stability due to the formation of electrical discharges. In the conducted research, the relation between the material composition of GEMs with their stability against discharges is studied. It is observed that the material choice can significantly affect the formation of secondary discharges, an unexplained and less frequent type of discharge in GEMs. Molybdenum is found to lead to a great improvement in stability. Furthermore, in a novel approach, the light emitted during GEM discharges is analysed via optical spectroscopy methods. Thus, material from the electrode layers is detected in the created plasma during discharges in GEMs but not in Thick-GEMs.

Secondly, a tracker system is developed using a module of scintillating fibers coupled with Silicon Photomultipliers, produced for the RadMap telescope project. The RadMap telescope is a compact radiation monitor system planned to be deployed to the International Space Station. In our studies, using the module with a Time-Over-Threshold based readout system is investigated. For this, Padiwa+TRB3 readout electronics, which were developed at GSI for the Hades experiment, are used. Various tests and calibration measurements were conducted with the assembled detector with finally the system being characterized during a beam test in the Paul-Scherrer-Institut. It was shown that the produced detector is capable of tracking minimum ionizing particles.

Together, the established discharge mitigation methods in GEMs and the development of the particle tracker system facilitate the construction and qualification of a photosensitive Thick-GEM detector capable of detecting visible light.

# Contents

|          |  |           |
|----------|--|-----------|
| <b>1</b> | <b>Preface</b>   | <b>1</b>  |
| <b>2</b> | <b>Characterizing GEMs and THGEMs with different electrode materials</b> | <b>2</b>  |
| 2.1      | Gas Electron Multiplier detectors . . . . .                              | 2         |
| 2.1.1    | Thick-GEMs . . . . .   | 4         |
| 2.1.2    | Discharges in (TH)GEM detectors . . . . .                                | 5         |
| 2.2      | Experimental setup and procedure . . . . .                               | 8         |
| 2.2.1    | GEMs and THGEMs with different materials . . . . .                       | 8         |
| 2.2.2    | Experimental setup . . . . .   | 10        |
| 2.2.3    | Stability against discharge studies . . . . .                            | 12        |
| 2.2.4    | Discharge light spectroscopy . . . . .                                   | 14        |
| 2.3      | Results . . . . .  | 17        |
| 2.3.1    | Observations in discharge light spectra . . . . .                        | 17        |
| 2.3.2    | Material dependence in discharge formation . . . . .                     | 22        |
| 2.4      | Discussion . . . . .   | 26        |
| <b>3</b> | <b>Development of a readout system for the RadMap telescope</b>          | <b>30</b> |
| 3.1      | The RadMap telescope project . . . . .                                   | 30        |
| 3.1.1    | Scintillating fibers . . . . .   | 32        |
| 3.1.2    | Silicon Photomultipliers . . . . .                                       | 33        |
| 3.2      | Development of the readout system . . . . .                              | 36        |
| 3.2.1    | ToT based Padiwa+TRB3 readout electronics . . . . .                      | 36        |
| 3.2.2    | System preparation and tests . . . . .                                   | 38        |
| 3.3      | Commissioning with a beam test . . . . .                                 | 49        |
| 3.3.1    | The experiment . . . . .   | 49        |
| 3.3.2    | Module gain calibration . . . . .  | 51        |
| 3.3.3    | Particle tracking . . . . .  | 53        |
| 3.3.4    | Detection efficiency calculations . . . . .                              | 54        |
| <b>4</b> | <b>Conclusion and outlook</b>  | <b>57</b> |
| 4.1      | ToT based trigger for THGEM photon detector . . . . .                    | 58        |
|          | <b>List of Figures</b>   | <b>61</b> |
|          | <b>List of Tables</b>  | <b>65</b> |
|          | <b>Bibliography</b>  | <b>66</b> |

# 1 Preface

Particle detectors have played a role in expanding our understanding of nature to an extent that few technologies have been able to do. Similar to the telescope, which has opened our eyes to the largest and furthest aspects of the cosmos, particle detectors have been successful in opening the door to the world of the smallest. The most precise theories to ever be developed in science have been confirmed by the measurements conducted by utilizing these devices. This success has of course only been made possible by the constant improvements and developments increasing the capabilities of various particle detector technologies. The instruments which are used today to measure the trajectories and properties of fundamental particles are greatly more precise and complex than the cloud chambers and photographic plates from the early days of particle physics. Still, the century-old effort of advancing these technologies further is far from over.

Presently, there are numerous vastly different types of particle detectors with many parts and constituents. From the interaction between the particle and the detector material to the amplification of the signal induced by the particle, finally to the recording of the signal, many steps are required to be taken when designing a particle detector. How these steps are achieved of course directly determines the performance of each detector technology and thus are investigated to a great extent. Still, the physics performance of a detector technology is not the only criteria to be considered. The production of the instruments, their deployment and operation in experiments, and the costs associated with all these are some examples of other non-trivial obstacles being tackled and improved upon.

In line with this global effort, two research projects, aiming to investigate and develop methods and tools to be used in various particle detector applications, are presented in this thesis. In the first part, the working principles of Gas Electron Multiplier (GEM) detectors [1] and their limitations due to the formation of electrical discharges are introduced. The mechanisms leading to the development of these GEM discharges are discussed and further investigated by utilizing optical spectroscopy methods. Moreover, the relation between the material composition of GEMs and their discharge stability is explored. In the second part of this thesis, the RadMap project [2], an undertaking aiming to deploy a state-of-the-art particle detector for radiation monitoring in the ISS is introduced. Furthermore, the development of a new particle tracker is presented, which incorporates modules from the RadMap telescope operated with a Time-over-Threshold based readout system. The electronics used in the readout and the various studies conducted with the assembled tracker are also presented.

In conjunction, the findings from the studies on GEM detectors and the built particle tracker presented in this thesis act as stepping stones in an ongoing effort to develop visible light-sensitive GEM detectors.

## 2 Characterizing GEMs and THGEMs with different electrode materials

The following chapter represents the studies conducted on various innovatory GEM and Thick-GEM (THGEM) foils which are constructed with electrodes using non-standard materials. The goal of the performed research is to determine how the material composition of GEM and THGEM foils can effect their performance in terms of stability against electrical discharges. Moreover, by studying discharge formation in these novel foils it is aimed to shed new light on even now unidentified mechanisms that lead to specific types of discharges observed in (TH)GEM detectors. For this, the produced foils are characterized and compared in respect to their stable operational limits. In addition, the light emitted during GEM and THGEM discharges is analysed using optical spectroscopy, which is an unprecedented approach in the scope of GEM discharge studies.

### 2.1 Gas Electron Multiplier detectors

Particle detectors are utilized in many different experimental environments ranging from compact radiation telescopes deployed on space probes to enormous particle trackers built-in particle collider complexes buried many meters underground. Moreover, the goal of the experiments they are a part of can be vastly different. As such, there are several different types of detector architectures and technologies, each with its strengths and potential drawbacks. One prominent type, which has seen wide use throughout the years, is gaseous ionisation detectors.

One of the earliest invented methods of detecting particles, gaseous ionisation detectors make use of the fact that high energy charged particles and radiation can ionize atoms on their path as they transverse a gas medium. Ionisation occurs when an electron is liberated from the atom leading to a free electron and a positively charged ion. By achieving a method to capture and record the positions of these ionisations it is possible to reconstruct the path of the incident ionizing particle, which in turn can be used to determine many more of its properties. However, the ionised gas atoms are not naturally stable. The fact that the ion and the electron are oppositely charged, leads to the fact that even after their initial separation, they will still attract each other and recombine. To circumvent this, gaseous ionization detectors utilize an applied electric field that is strong enough to overcome the Coulomb attraction between the ion and the electron causing them to remain separated and drift apart. The drifting ions and electrons can subsequently approach a readout electrode on which they induce an electric signal, which can be registered by dedicated readout electronics. The number of ionisations and thus the number of primary electron-ion pairs that are

## 2 Characterizing GEMs and THGEMs with different electrode materials

created from an incident particle is few. Therefore, an amplification of the signal is necessary. In proportional counter detectors, this amplification is achieved in form of a multiplication of the created primary electrons proportional to the initial number by the Townsend avalanche process. In the presence of strong electric fields, primary electrons are accelerated to the extent that they acquire enough energy to ionize further gas atoms. This applies also to the newly liberated electrons which results in a cascade of ionization. With this, a single initial primary electron can cause the inception of an electron cloud, which induces a much stronger signal as it drifts towards the readout electrode.

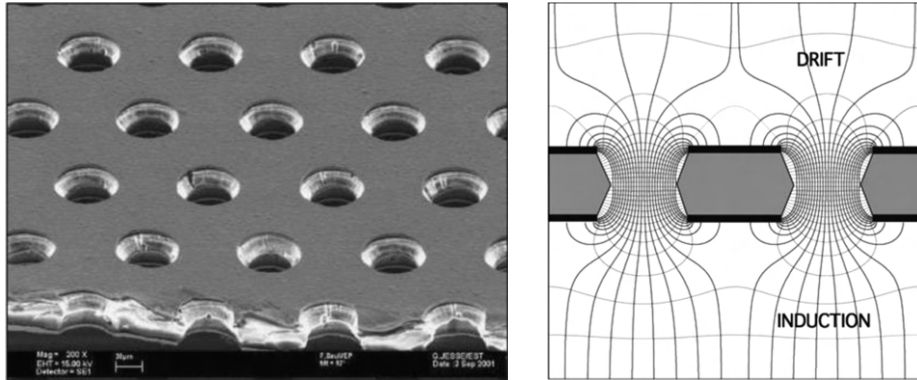


Figure 2.1: (left) Picture of a GEM foil section captured with an electron microscope. The conical GEM holes with a diameter of  $70\ \mu\text{m}$  and the individual layers making up the  $50\ \mu\text{m}$  thick foil can be recognized. (right) Sketch depicting the cross-section of GEM foil holes. The electric field enhancement inside the hole due to the geometry of the structure is also shown. [3]

For the avalanche multiplication to occur, high electric fields approaching the breakdown potential of the used gas are required. Achieving such strong fields is made easier by having a non-uniformly applied electric field geometry, where the electric field is locally much stronger in certain specific amplification regions. In Gas Electron Multipliers (GEM) this is the case inside the GEM holes. GEMs were developed by Fabio Sauli in 1997 [1]. They incorporate  $50\ \mu\text{m}$  thin polyimide foils with conductive cladding layers on both sides and many  $50\ \mu\text{m}$  ( $70\ \mu\text{m}$ ) inner (outer) diameter through holes arranged in a hexagonal pattern with a pitch of  $140\ \mu\text{m}$ . A moderate electric potential applied between the two conductive layers acting as electrodes leads to a strong electric field inside the holes as shown in Figure 2.1. The electric field inside the holes enables the avalanche multiplication of the primary electrons arriving at the GEM. The developed electron cloud is in turn extracted from the GEM holes on the bottom side of the foil and then collected on a readout anode. The readout electrode is usually segmented in small pads or strips which are read out separately enabling reconstruction of the tracks from the incident particle with high spatial resolution.

The fact that the amplification structure is in the form of a foil in GEM detectors brings about many advantages such as intrinsic ion backflow suppression, which lead to the wide use of the technology in many high energy physics experiments. The GEM detector is highly scalable and can be integrated to cover large areas cost-effectively.

Although producing large area GEM foils with uniform hole properties is challenging, it is possible to position GEM foils side-by-side to cover larger areas with minimal blind zones. Moreover, it is possible to place multiple GEM foils on top of one another in a stack configuration which enables to have multiple avalanche multiplication steps from the same primary signal, leading to higher achievable signal amplifications [4]. Finally, GEMs are very radiation tolerant, meaning that they can be installed and operated in environments with high radiation fluxes (upto  $10^8 \text{ Hz cm}^{-2}$  [5]). These facts are being utilized in large particle physics detectors such as the ALICE TPC [6] and the CMS Muon Endcap[7] where GEMs are used as the amplification structures.

### 2.1.1 Thick-GEMs

Another type of particle detector technology based on the principles of Gas Electron Multipliers is the Thick-GEM (THGEM). As suggested by the name, THGEMs replace the thin GEM foils with thicker THGEM foils. This increase in dimension is usually in the order of magnitude for the insulating core and the conducting cladding layers as well as the diameter of the holes on the surface. A comparison between the geometries of a GEM and THGEM foil is given in Figure 2.2. The increased dimensions lead to the THGEM structure having an overall much sturdier build. As such, THGEMs don't suffer some of the problems associated with GEMs such as sagging, where the electrostatic forces between the GEM foils in a stack configuration lead to warping of the thin foils. This in turn affects the field geometry in the gaps between the foils reducing the overall performance and stability of the detector. Another foremost advantage of THGEMs is the simplicity of their construction. Whereas for GEMs a lot of chemical etching and masking procedures are required to reliably create the micrometre sized holes, THGEM holes can simply be mechanically drilled. Furthermore, the sturdier build of the THGEM foil design increases the robustness of the detector against many potential hazards such as dust induced shorts or discharges.

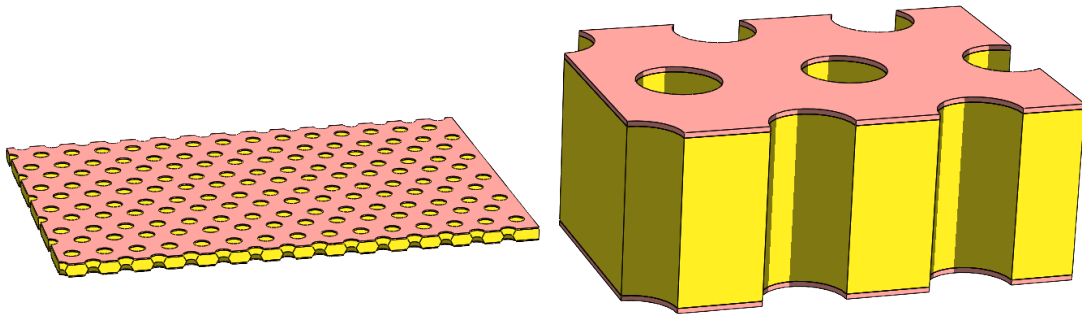


Figure 2.2: Side-by-side comparison between standard GEM and THGEM foil cross-sections.

However, there are also drawbacks associated with THGEMs, such as the significantly more prominent charge up. The charge-up phenomenon concerns the charge accumulation on the surface of dielectric materials and has been widely studied in many Micro-Pattern-Gaseous-Detectors over the years [8, 9]. Usually, with the thin

GEM foil geometry, this process reaches an equilibrium in the order of seconds after the change of the applied potentials [10]. However, with the increased thickness of the THGEM, the inner surface of the dielectric material is also significantly increased. This leads to the observation of a charge up period in the order of hours or days, during which the amplification achieved inside the hole is affected. This leads to a gradual variation of the gain performance of the detector up to a factor of 2 [11, 12]. As such, it is impractical to utilize THGEMs in experiments where frequent changes in operational parameters are required. In addition to the charge up, THGEMs should lead to lower spatial resolution compared to GEMs due to the lower hole density. In practice, however, the effective spatial resolution of a (TH)GEM detector is mainly determined by the design of the readout electrode and the diffusion properties of the used gas mixture [13]. Another performance criteria, in which the THGEM design is worse, is the stability of the detector against the formation of electrical discharges during operation. This phenomenon is discussed below in Section 2.1.2.

### 2.1.2 Discharges in (TH)GEM detectors

The study of electrical discharges in gaseous media is a widely investigated subject, where the term "discharge" can refer to different phenomena in different communities. In general, a gas discharge indicates the flow of current through a gas medium that is not in normal conditions conductive. In the presented work, however, discharge refers to the spark event resulting from an electric breakdown inside the gas volume which is associated with the formation of a plasma channel in the gas accompanied by a temporarily high current flow and an optical and acoustic signal. Such events are observed to occur in GEM detectors during operation and are among the leading factors limiting the gain with which the detector can be operated stably. When GEM discharges occur, they lead to a sudden drop in the applied potentials and render the detector temporarily blind until the foil charges up again. Furthermore, it is also possible that GEM foils or the readout electronics can be damaged by a discharge. With these facts in mind, it is impossible to ignore discharges and it is crucial to mitigate them. As a result, there has been an extensive effort investigating GEM discharges and developing mitigation methods.

GEM discharges can be separated into two distinct categories. Primary discharges occur inside GEM holes and secondary discharges occur in the gap between GEM foils or between a GEM foil and the readout anode. Figure 2.3 visualizes these two types of discharges and shows the distinctive signals they induce on the readout anode. Primary GEM discharges are much more common compared to secondaries and are therefore better studied. Since they occur inside the GEM holes primary discharges may lead to a short between the top and bottom GEM electrodes, leaving the involved GEM foil inoperable.

To avoid such issues during operation, there are multiple methods aiming to mitigate the formation of primary discharges. Firstly, it is observed that GEM holes with surface imperfections inside and around them, acting as primary discharges hot-spots, are less stable [14]. As such, the uniformity of the holes on a GEM foil is very important and recent developments in the manufacturing procedures and steps are currently

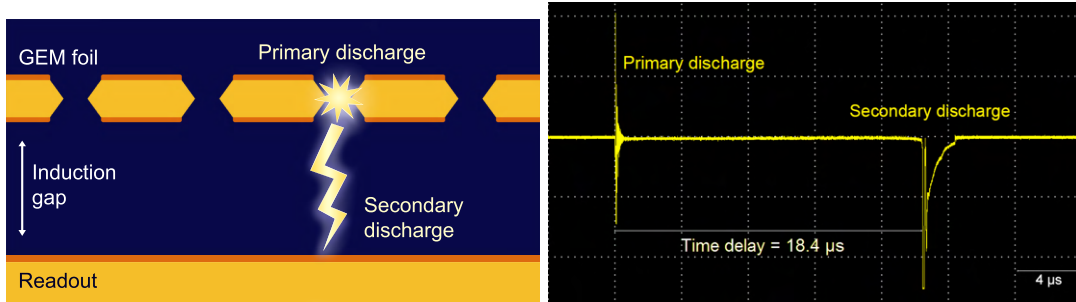


Figure 2.3: (left) Scheme of a GEM detector portraying a primary discharge that occurs inside a GEM hole, followed by a secondary discharge developed in the gap between the GEM and the readout electrode. (right) Electrical signals induced by different types of discharges on the readout plane.

capable of producing large area GEM foils with negligible defects [15]. Secondly, to minimize the energy released during a discharge, the capacitance of a GEM needs to be reduced. It was shown in [4] that segmenting the foil into sections no larger in area than  $10 \text{ cm}^2 \times 10 \text{ cm}^2$  can significantly reduce the occurrences of shorts. Similarly, adding decoupling and protection resistors on the High-Voltage (HV) scheme powering the foil segments also helps avoiding damages caused by occurring discharges [4]. Further discharge mitigation methods include the optimization of the used gas mixture by incorporating a quencher [16], and stacking of multiple GEM foils and operating each of them at relatively low potentials [4]. By incorporating these approaches in the design process of a GEM detector, it is possible to operate stably with high gains in the order of  $10^5 - 10^6$  [3].

With this, it can be assumed that the problems associated with primary discharges are practically solved. Still, to further push the capabilities of our detectors, it is crucial to first understand why and how this phenomenon occurs, so that this knowledge can in turn be used to develop new and better techniques and structures. To this point, the understanding of primary discharges is also rather solid.

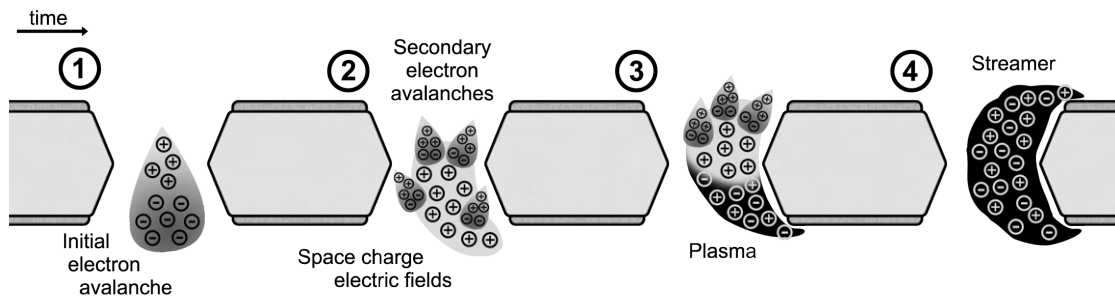


Figure 2.4: Sketch depicting the evolution of a streamer discharge. A conductive plasma channel between the top and bottom GEM electrodes is formed leading to a breakdown. [17]

Figure 2.4 depicts the streamer discharge process in GEMs. A streamer is caused by

the local electric field enhancement due to the proximity of many space charges. In GEMs, after the primary electrons lead to the formation of a large electron cloud with the Townsend avalanche, an equal number of ions is also generated. Due to fact that these ions drift and diffuse much slower than electrons, the avalanche process leaves behind a bunch of positive charge carriers inside the hole. When the charge limits are exceeded the local electric field around this ion cluster becomes large enough that further ionisations occur around it. The ions still following the ambient electric field, drift towards the GEM top electrode. As the streamer moves and grows it creates a channel with many free charge carries on its path. Finally, when the streamer reaches the top GEM electrode, there is a highly conductive plasma channel between the top and the bottom electrodes which triggers a spark discharge. The requirements leading to the initial creation of the streamer are also well understood. It is shown for GEMs and THGEMs that when the number of charge carriers inside a hole exceeds a certain limit a streamer will develop leading to a discharge. The limit is determined to be for both geometries in the range of  $(5 - 9) * 10^6$  [18, 19, 20, 21]. With all of this in mind, the activation and the development of primary discharges are also well understood in addition to the availability of methods for their mitigation. This is, however, not the case for secondary GEM discharges.

Secondary discharges in GEMs are breakdown events in the gap between a GEM foil and the subsequent electrode (another GEM or readout electrode). And, as the name suggests, they occur as follow up events to primary discharges. Although they are less frequent, they are usually more dangerous for the detector. This is because, secondary discharges release more energy and the readout electrode, to which fragile readout electronics are connected, can be involved. Similar to primary discharges, HV scheme optimization [22] and other methods can be used to mitigate the formation of secondary discharges. Concerning our understanding of the formation of these events, there is much less clarity compared to primary discharges.

Secondary discharges occur after and in the region around the initial primary discharges, thus it can be concluded that a discharge propagation mechanism triggers their formation. Propagation of discharges is also a previously commonly observed phenomenon in many other gaseous ionization detectors such as Multi-Wire-Proportional-Chambers (MWPC) [23]. The established mechanism in those systems concerns the VUV photons emitted during the primary spark. Further ionisations can be caused by such photons which can trigger the development of a streamer in the gap. This explanation is solidified by the observation that in those systems, the propagation event happens within nanoseconds, practically without any time delay, which concurs with light-induced ionisations. However, with GEMs, a substantial time delay in the order of tens of microseconds is observed between the primary and secondary discharges. Furthermore, this time delay depends on the used gas mixture and applied field configurations [24]. These facts cannot be explained with any propagation mechanisms involving photons [25]. Another idea concerns the emission of secondary electrons from the bottom surface of the GEM foil after a primary discharge. Electrons may be liberated by thermionic emission processes due to the heat generated around the discharging hole, or by ions approaching the foil surface [24]. With such a method, it would be possible to explain the observed time delays as the required accumulation

duration of the emitted charges to reach a certain limit. Observations of persisting thermal activity around GEM holes long after the initial discharge also further support this explanation [25, 26]. However, other observations such as the development of secondary discharges with an inverted field below the GEM (where the emitted electrons would no longer drift towards the gap and not accumulate) illustrate that there is more to the story of secondary discharge formation [24]. Therefore, it becomes clear that new observations, which shed new light, are required for solving this puzzle. With this motivation, the work conducted in this thesis described below aims to study the formation of secondary discharges using novel approaches, such as utilizing optical spectroscopy to analyse the light emitted during GEM discharges or testing (TH)GEMs with non-standard materials.

## 2.2 Experimental setup and procedure

In the presented studies, the performance of multiple GEM and THGEM foils ((TH)GEM) with conducting layers composed of different materials are investigated. The foils are produced in a way that enables the use of a wide range of metals, which have so far never been used in the application of (TH)GEM detectors. The methods and apparatus used to study discharge formation in these foils are described in this section.

### 2.2.1 GEMs and THGEMs with different materials

Customarily, a (TH)GEM consists of an insulating foil that is clad with copper on both sides. Where the copper layers act as the electrodes between which an electric field can be applied. Multiple holes are etched or drilled through all the layers making up the foil within which the applied field is substantially amplified by the geometry of the hole. The ions generated during the avalanche multiplication process of electrons inside the hole is then mostly collected at the top GEM electrode layer. With this, this layer needs to exhibit a relatively high conductivity to mitigate the accumulation of ions. Which would otherwise lead to a long-term charge-up effect. Beyond this fact, there are initially no major fundamental constraints for the material choice making up the electrode layers in most GEM detector applications. In practice, however, it is the case that copper is used as the GEM electrode material of choice in most detectors. The main motivation behind the wide use of copper is its common use in the PCB industry and the abundance of techniques and know-how for producing GEM foil-like structures using it. The reliable production of structures with patterns in the micrometre scale remains to this day a big challenge. The research and development which would be required to produce large scale GEM foils with other materials are beyond the scope of most detector projects. Still, there have been singular cases of experiments using (TH)GEM foils with electrode layers consisting of materials other than copper. These include gold [27, 28], DLC [29] and chromium [30]. But, these examples are confined in applications where some known distinct properties of the material such as the work-function of gold and chromium, or the high resistivity of DLC is required for the performance. Thus, a thorough systematic study on the effects of material choice has so far not been conducted.

## 2 Characterizing GEMs and THGEMs with different electrode materials

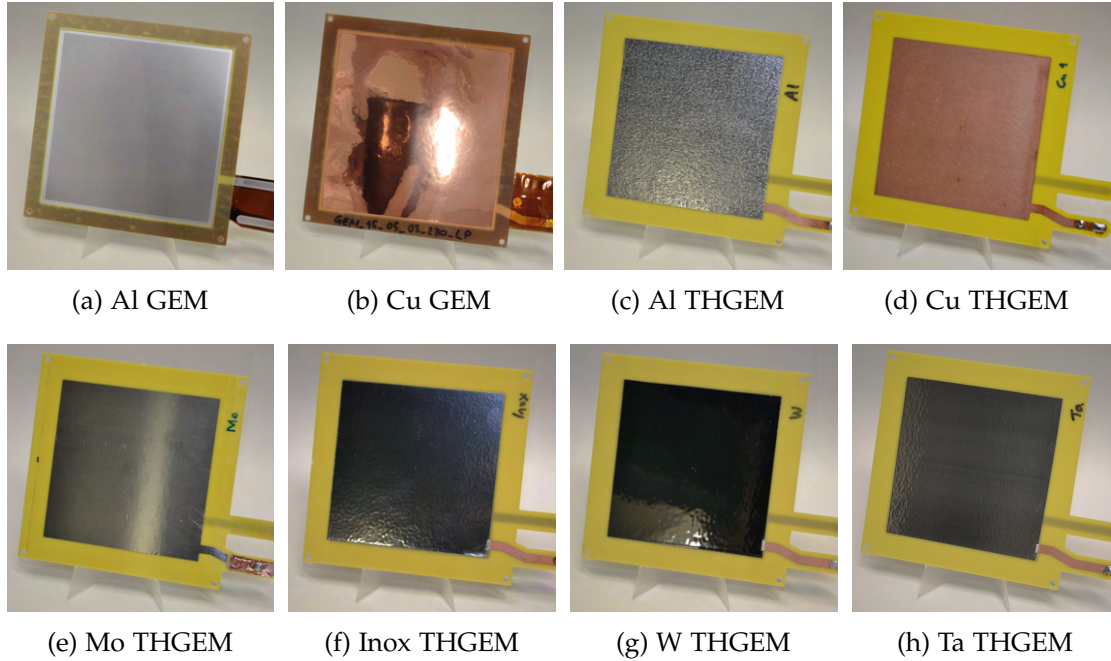


Figure 2.5: The used GEM and single-hole THGEMs.

With this motivation, in this study, the effects of the choice of material used for this conductive layer on the discharge performance is investigated. For this, we tested several single-hole THGEM and multi-hole GEM foils which incorporate other metals in place of copper. The tested materials include aluminium (Al), molybdenum (Mo), stainless steel (Inox), tantalum (Ta) and tungsten (W) in addition to copper (Cu). All the tested (TH)GEM samples have been produced in the CERN PCB workshop, the photos of which are given in Fig. 2.5.

The produced single-hole THGEM foils incorporate a  $800\ \mu\text{m}$  thick FR4 insulating layer sandwiched by  $25\ \mu\text{m}$  thick metal conducting layers on both sides. The metal films are cut from larger sheets to the required  $10 \times 10\ \text{cm}^2$  active area. A solid film of cast epoxy is used to adhere the metal films to the base FR4. A thermal-hydraulic press is used to cure the epoxy and ensure uniformity. As an exception, the tungsten THGEM incorporates a  $50\ \mu\text{m}$  thick metal layer due to the lack of thinner tungsten sheets. Moreover, the copper THGEM is produced using a standard PCB material which is supplied with a  $35\ \mu\text{m}$  copper cladding. After glueing of conductive layers, the THGEM boards are then drilled in the centre to create the amplification hole with a diameter of  $400\ \mu\text{m}$ . The hole has a cylindrical shape without any rim. The THGEMs are then put into a series of chemical baths aiming to clean and remove surface imperfections.

The choice of the employed metals was done in a way to cover a large range of thermal and mechanical material properties. The relevant material properties such as conductivity, melting temperature and work function are summarized in Table 2.1.

In addition to the introduced single-hole THGEMs, also standard multi-hole GEMs with copper and aluminium cladding are tested in this study. For reliable operation

---

<sup>1</sup>value for iron

## 2 Characterizing GEMs and THGEMs with different electrode materials

Table 2.1: Properties of the coating materials employed in this study [31, 32].

| Material | Conductivity<br>( $10^6 \text{ S m}^{-1}$ ) | Work function<br>(eV) | Melting point<br>( $^{\circ}\text{C}$ ) | Boiling point<br>( $^{\circ}\text{C}$ ) | Thermal conductivity<br>( $\text{W m}^{-1} \text{ K}^{-1}$ ) | Density<br>( $\text{g cm}^{-3}$ ) |
|----------|---|-----------------------|---|---|--|-----------------------------------|
| Al       | 36.9  | 4.08                  | 660                                     | 2470                                    | 237  | 2.702                             |
| Cu       | 58.7  | 4.7                   | 1083                                    | 2575                                    | 386  | 8.96                              |
| Inox     | 1.37  | 4.4                   | 1510                                    | 2750 <sup>1</sup>                       | 16.3   | 7.85                              |
| Mo       | 18.7  | 4.5                   | 2623                                    | 4651                                    | 138  | 10.22                             |
| Ta       | 7.6   | 4.22                  | 3317                                    | 5365                                    | 57.5   | 16.65                             |
| W        | 8.9   | 4.5                   | 3422                                    | 5550                                    | 174  | 19.35                             |

GEMs require intricate patterning of very small features during production. This was not possible to recreate with the mentioned harder metals (Mo, Inox, Ta, W). This is why only copper and aluminium standard geometry GEM foils were produced.

The two GEM foils incorporate a  $50 \mu\text{m}$  Apical insulating layer clad with  $5 \mu\text{m}$  thick copper or aluminium. For the production of the copper GEM, a thin ( $0.1 \mu\text{m}$ ) layer of chromium is used to adhere the copper to the Apical base. Using photo-lithography, a hexagonal hole pattern with a pitch of  $140 \mu\text{m}$  is marked on the active area of the foil, which in turn is etched to produce the GEM holes. The created double-conical holes have an inner diameter of  $50 \mu\text{m}$  and an outer diameter of  $70 \mu\text{m}$ . Similarly, for the production of aluminium GEM, the same process as for the standard copper-cladded foil is used to create the hole structure in the Apical layer. Afterwards, however, the copper and chromium are completely removed and a  $10 \mu\text{m}$  layer of aluminium is applied by Physical Vapour Deposition. An acid etch is then used to remove the aluminium from the holes selectively resulting in approximately  $5 \mu\text{m}$  aluminium electrodes.

After their production, all GEM and THGEM foils are visually inspected for imperfections and are tested by applying high electric potentials ( $600 \text{ V}$ ) between the top and bottom electrodes to check for shorts and residual contamination. Additionally, holes of all THGEM foils were studied under an optical microscope to exclude any local defects or differences in geometry, which would lead to a different discharge performance of the foils. Figure 2.6 shows microscope pictures of all six THGEM holes taken after the discharge measurements. No obvious defects can be found, however, for future reference, it might be of interest to investigate the samples using also an electron scanning microscope.

### 2.2.2 Experimental setup

The measurements presented in this chapter are conducted in the GEM laboratory in the Physics Faculty of TUM. For the operation of the studied GEM and THGEM detectors, two main systems are required. First, a gas system for the mixing and flushing of the noble and quencher gases is used. This includes the gas cylinders containing the pure gases which are to be mixed, a pressure reducer on all gas lines, a calibrated gas mixer module where the wanted mixing ratio can be set and a flow controller. Additionally, a Cambridge Sensotec Rapidox 3100 gas sensor is used for monitoring the flow rate, gas

## 2 Characterizing GEMs and THGEMs with different electrode materials

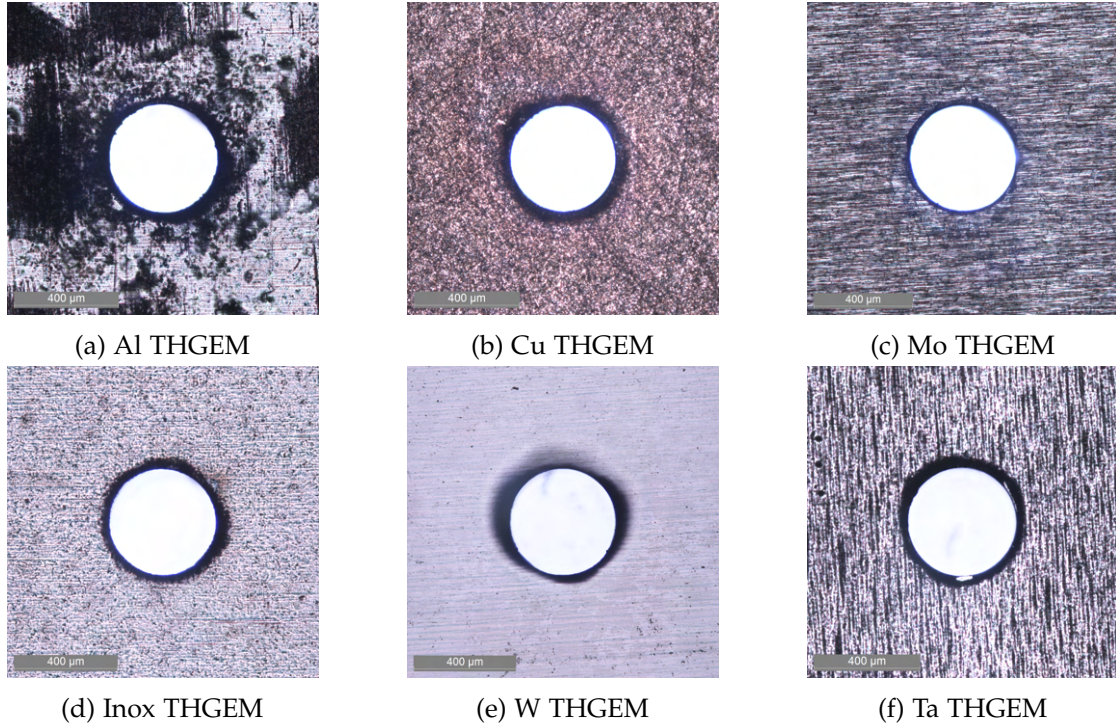


Figure 2.6: Microscope images of the THGEM holes seen from the induction side.

overpressure and impurities like oxygen and water in the gas. During the conducted measurements an oxygen contamination below 20 ppm and a humidity contamination below 100 ppmV is sustained. Second, a high-voltage (HV) system is required to apply the potentials (ranging up to 4 kV) to the various electrodes inside the detector. For this, a multi-channel power supply from the company ISEG is used with grounding resistors on each channel connected by SHV cables. The detector is composed of a dedicated gas-tight vessel, as seen in Figure 2.7, with a built-in BOROFLOAT window on one side for optical measurements. The detector vessel is placed throughout the measurement campaign inside a large copper box which primarily acts as a Faraday cage mitigating electromagnetic interference, in addition to acting as a dark optical enclosure diminishing environmental light background.

Moreover, several apparatus are used for the monitoring of the detector setup. The used power supply incorporates sensors measuring the applied potentials and current levels. In addition to this, a PicoLogic PA125-24 pico-ammeter module [33] is also used in a series configuration for more precise monitoring of the flowing currents on all channels. Also, an oscilloscope is connected to the anode electrode to record the time evolution information of fast signals such as sparks, which is lost to the long integration time of the pico-ammeter. Finally, for the conducted spectroscopy studies, an OceanOptics QE65000 spectrometer is used, which is sensitive to light in ultraviolet, visible and near-infrared (UV-VIS-NIR) range. An optical fibre light-guide of 600  $\mu\text{m}$  diameter is connected to the entrance aperture of the spectrometer. A collimation lens is attached to the other end of the fibre. The lens is mounted to a 3D printed structure

## 2 Characterizing GEMs and THGEMs with different electrode materials

fixed to the gas vessel and is positioned centrally to the window facing directly towards the anode electrode inside.

Inside the detector vessel are the drift cathode, the anode readout, and the (TH)GEM foil under investigation is mounted using plastic pillars and spacers. These mounting structures enable the easy disassembly and the easy swapping of (TH)GEM foils. The distance between the cathode and the top side of the (TH)GEM, called the drift distance is kept at 27 mm. Also, the induction distance between the bottom side of the (TH)GEM and the anode is kept at 2 mm. These values are taken to be comparable with other related studies conducted with (TH)GEM detectors [24, 18, 21]. All the used electrodes and foils have an active area of  $10\text{ cm} \times 10\text{ cm}$ . The cathode incorporates a 5 mm radius hole in its centre. A mixed alpha source ( $^{239}\text{Pu} + ^{241}\text{Am} + ^{244}\text{Cm}$ ) is mounted on top of the cathode PCB shooting into the drift volume through the hole. The readout anode consists of a fine mesh. This is done to have a direct line of sight to the bottom side of the (TH)GEM foil from outside the window, while also maintaining a uniform induction field. The used mesh has an optical transparency of 50 %.

For the conducted discharge studies presented in Section 2.3.1, the detector is flushed predominantly with Ar-CO<sub>2</sub> (90-10). In addition tests with pure argon and pure neon are also conducted as reference in the spectroscopy studies. Relevant properties of Ar-CO<sub>2</sub> (90-10) include a density of  $1.8 \times 10^6\text{ g/cm}^3$ , an effective ionization energy of 28.8 eV, and an electron drift velocity of 3.25 cm/ $\mu\text{s}$  at normal temperature and pressure conditions (NTP) and at an applied electric field of 400 V/cm and no magnetic field [34].

### 2.2.3 Stability against discharge studies

The measure for determining the long term stable operability of a detector is given as its stability against the formation of electrical discharges. This is determined by the measurements of primary and secondary discharge probabilities as a function of the applied field configurations or the resulting gain. Primary discharge probability ( $P_1$ ) is calculated by the discharge rate ( $R_1$ ) normalized to the rate of the radioactive source ( $R_{\text{Src}}$ ) as given in Equation 2.1.

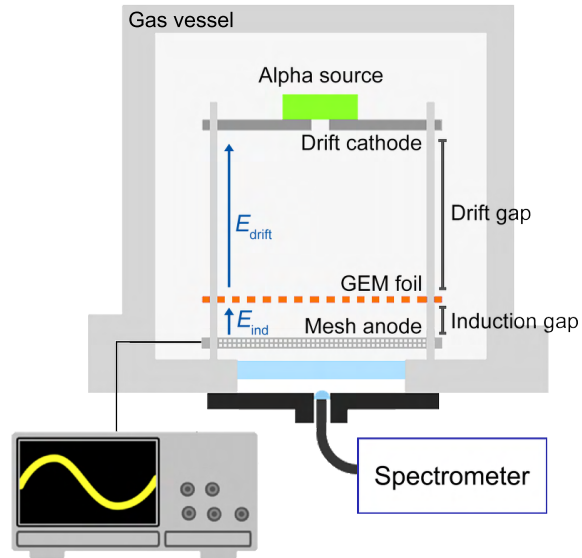


Figure 2.7: Schematic picture of the experimental setup and the detector geometry.

$$P_1 = R_1/R_{Src} \quad (2.1)$$

$R_1$  is measured by recording and identifying the signals of primary discharges at the readout electrode using an oscilloscope. The number of the observed sparks, as well as the duration of the measurement, is then used to determine the rate.  $R_{Src}$  is determined by recording the energy spectrum measured with the detector using an Analog-to-Digital-Converter. The number of hits belonging to the peak associated with the energy of the used source is then normalized by the measurement time. Primary discharge probability is usually given as a function of the gain, as this is the main parameter relevant for discharge formation. However, in the case of the single-hole THGEM foils used in these studies, the gain can not properly be defined. This is because there is a single-hole on a large surface, and most of the primary electrons do not enter the THGEM hole. With this, the collection efficiency, the ratio of the primary electrons that go inside GEM holes, of 100% clearly cannot be assumed and measuring it is not feasible with the low primary currents expected from the used source. For this reason, primary discharge rates are given as a function of the applied voltage across the foil. The gain is known to be exponentially proportional to the applied potential [1], as such it is an adequate measure of the achieved detector amplification.

The secondary discharge probability ( $P_2$ ) is given by the ratio of events with secondary discharges  $N_2$  to all recorded primary discharge events  $N_{Total}$ , as given in (2.2). An oscilloscope is utilized for recording the events by triggering on the initial positive rising-edge of the primary discharge signals (as shown in Figure 2.3). In addition, events where the signal goes below a threshold, which is only exceeded by secondary discharge signals, are counted.

$$P_2 = N_2/N_{Total} \quad (2.2)$$

It has been shown that the formation of secondary discharges depends on the applied induction field between the bottom side of the foil and the anode electrode [24]. Considering these results, the secondary discharge probability is measured as a function of the applied induction field.

Finally, the time delay between the primary and the secondary discharges in an event is calculated. This is again done automatically by triggering on the rising edge of the primary discharge signal with an oscilloscope and measuring the duration until the signal drops below a certain voltage level associated with the initial falling edge of a secondary discharge signal.

### 2.2.4 Discharge light spectroscopy

In addition to the discharge stability studies, also optical spectroscopy is utilised as a novel probe for investigating discharges in the used (TH)GEMs. For this, the light emitted during the discharges is collected with a collimating lens and optical fibre which in turn is analysed with a UV-VIS-NIR Ocean Optics QE65000 [35] spectrometer. More details on the measurement setup are given in Section 2.2.2.

The spectrometer is operated with a 10s exposure duration. Within a single measurement the light from multiple discharges is recorded and integrated. The relatively long exposure time is chosen to compensate for the low light emission intensity of single discharges. The number of discharges that occur during the exposure are counted with an oscilloscope (as described in Section 2.2.3). The measured spectra are thus normalized to the number of recorded discharges. To compensate for the effects (e.g. intensity response) introduced by the used light guide apparatus, it is crucial to calibrate the recorded spectra in wavelength and intensity.

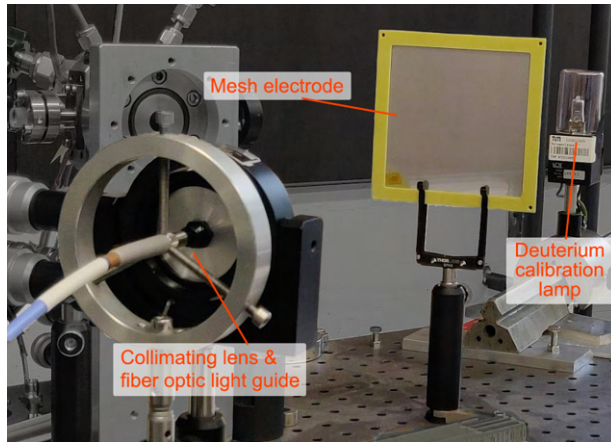


Figure 2.8: Deuterium lamp setup used to measure the absolute intensity calibration.

For the intensity calibration, a reference deuterium lamp with a known emission spectrum is used. The lamp is placed at a distance of 100 cm, shown in Figure 2.8. Since the absolute irradiance values of the lamp are given for this distance. The light spectrum from the lamp is then measured using the same setup. The obtained spectrum (given in Figure 2.9) is compared to the irradiance data provided by the manufacturer from which the absolute intensity calibration of the setup is determined.

Similarly, a wavelength calibration is also required. This is achieved by measuring discharge light spectra in THGEMs. An example of such a spectrum acquired with the Al THGEM is shown in Fig. 2.10. The observed peaks can be associated with the emission lines of the used gas mixture components and other contaminants [36]. The positions of these peaks are then determined by fitting them using a pseudo-Voigt function and taking the mean. The obtained peak positions are in turn compared to known values of emission line wavelengths from spectroscopy databases [37]. The observed shift between the measured and literature values is used to create a wavelength calibration. Finally, during each measurement session, blank spectra are taken to obtain and later remove the background light pollution in the detector and noise from the spectrometer pixels. With these steps in place, the measured spectra of discharge light can be properly investigated and analysed.

In the conducted studies, the main focus lies with the identification of the characteristic emission lines of the elements abundant in the created discharge plasma. As

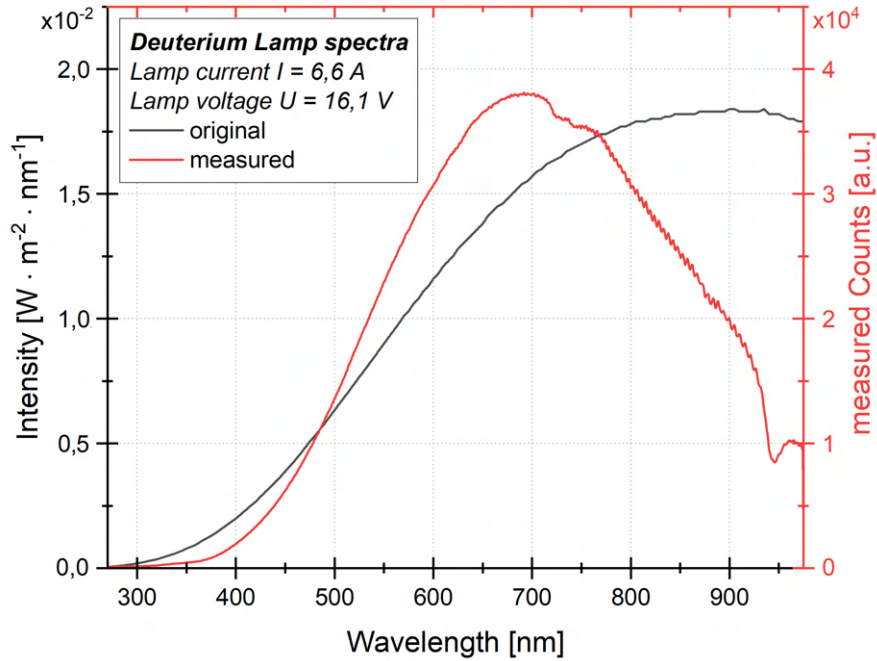


Figure 2.9: The measured and manufacturer provided spectra of the used calibrated Deuterium lamp. The observed difference is due to the intensity response of the various components in the setup.

such, only the sharp peak structures are relevant for the analysis, meaning that the background of the spectra can be ignored. The background continuum in the presented spectra are due to the broad emission spectra of the used quencher gas. This can be recognized in Figure 2.10 where the background distribution is significantly lower when discharges with no quencher are observed. To reduce muddling due to different background shapes in different measured spectra, all spectra shown in Section 2.3.1 are background subtracted. The background distribution is fitted using the algorithm and the MATLAB tool described and provided in [38]. The method employs wavelet transforms to fit the emission peaks in the spectra. Wavelets are localized wave-like oscillations which unlike waves are only non-zero in a short interval as such can extract local spectral information more efficiently compared Fourier transform. In our case, the Biorthogonal 3.7 function is selected as the wavelet type for this step, as it yielded the best results for our spectra. In the iterative procedure, the algorithm subtracts the fitted peaks above the background level. After ten iterations, the resulting fit distribution converges to the real background distribution. This fit is later subtracted from the original data leading to the background-less spectra. An example spectrum of copper GEM discharges in Ar-CO<sub>2</sub> (90-10) before and after the background subtraction is shown in Fig. 2.11.

With all the described processing applied, a resolution of  $\sim 1.5$  nm (FWHM) can be extracted for the peaks in the given spectra. This value is comparable with the optical resolution of the spectrometer given by the producer (0.14 nm to 7 nm), which depends on the used slit size [35]. An additional final normalization step is also done in certain

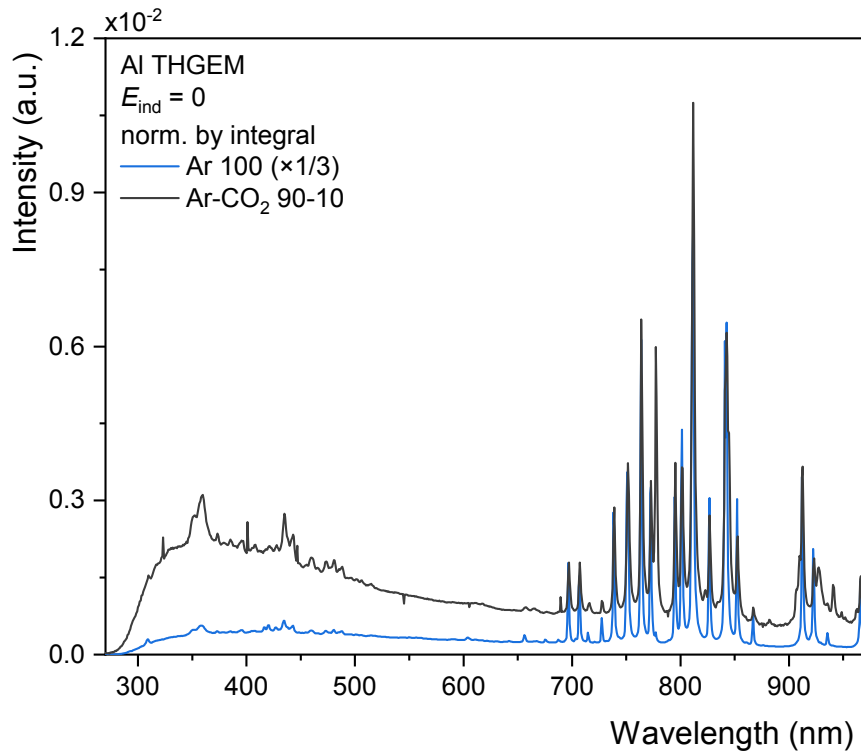


Figure 2.10: Discharge light spectra of Aluminium THGEM discharges measured in Ar-CO<sub>2</sub> (90-10) mixture and pure argon. The blue spectrum is scaled down by a factor of 1/3. See text for details.

plots designated with "norm. by integral" in their legend. It was observed that the mounting structure used for the collimating lens in the setup is prone to small shifts, which leads to a variance in the absolute light intensity measured on different days. As only the position and not the absolute intensity of the peaks are relevant to the conducted studies, the spectra in the presented figures are normalized by their integral (total counts). This enables the corrected figures with multiple spectra to be more easily viewed, where individual spectra can be more accurately compared.

The spectroscopy studies of GEM and THGEM discharges presented in Section 2.3.1 are predominantly conducted with Ar-CO<sub>2</sub> (90-10), since a lot of the research on GEM discharges has been conducted with this gas mixture [18, 24, 25, 39, 17]. However, as can be seen in Figure 2.10, many of the observed emission lines in the spectra are associated with the used noble gas. Therefore, it is important to also analyse discharge light from a different noble gas, where the resulting spectrum can be used to confirm the correct identification of all argon emission lines. For this, measurement using pure neon is conducted and compared against the spectrum obtained with pure argon in Figure 2.12. As can be seen, the spectra consist of a number of different emission peaks which are associated with the used noble gases accordingly.

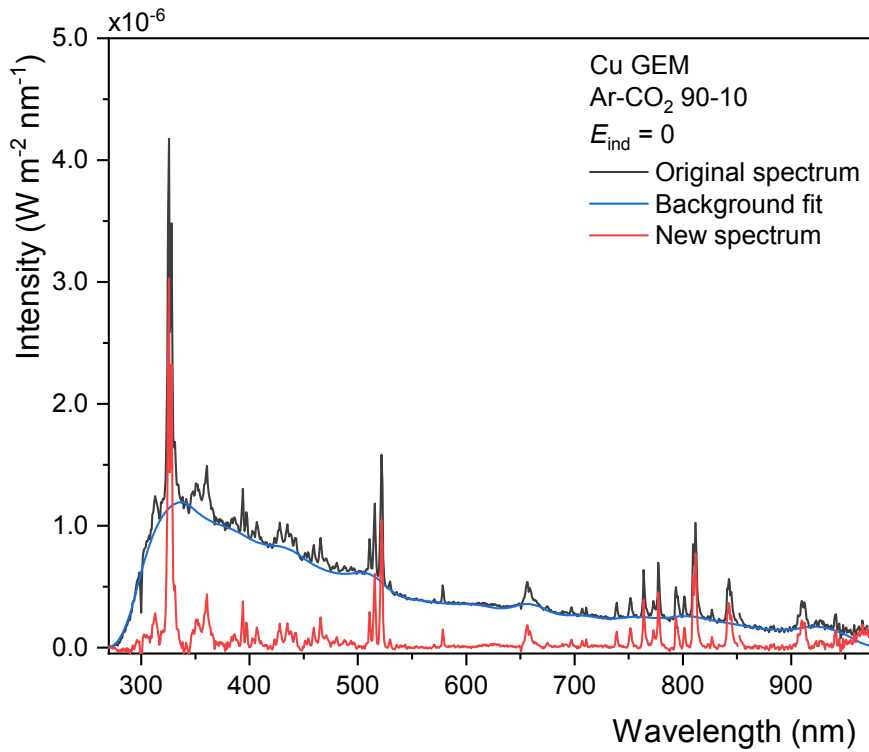


Figure 2.11: Example of the background removal procedure for a copper GEM discharge spectrum. The continuous background of the original spectrum (black) is fitted (blue) and subtracted. The red plot shows the resulting spectrum after background subtraction. See text for details.

## 2.3 Results

### 2.3.1 Observations in discharge light spectra

#### GEM foils with Al- and Cu-cladding

First and foremost the primary discharge light spectrum of a standard geometry copper GEM operated in Ar-CO<sub>2</sub> (90-10) gas mixture is shown in Fig. 2.13. It is possible to identify emission lines associated with copper in the shorter wavelength region of the plot, whereas longer wavelengths are dominated by the emission lines from the used noble gas argon. Some of the smaller observed peaks are attributed to oxygen, carbon and hydrogen. Their presence is explained either as components of the used quencher CO<sub>2</sub> or as contaminants in the chamber, such as residual amounts of H<sub>2</sub>O and O<sub>2</sub> in the gas (see Section 2.2.2). Especially significant is the observation of copper lines which points to the vaporization of the electrode material during the discharge process. It is important to note that the narrow emission lines, as are visible in the spectrum, can only originate from free particles in the discharge plasma. Atoms contained in the crystal lattice of the bulk foil material would only lead to a broad band emission instead of single lines [40]. For this reason, it is concluded that the GEM electrode material is vaporized during the discharge process. Previously, the vaporization of GEM foil

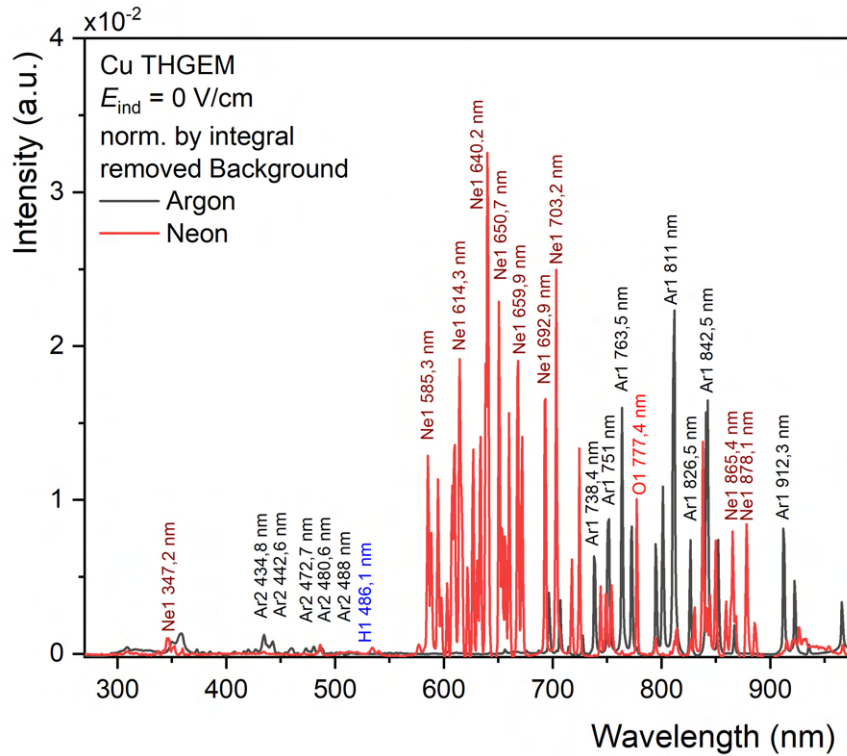


Figure 2.12: Primary discharge light spectra of a copper THGEM operated with pure argon and pure neon. The emission lines associated with the noble gases are designated.

material had only been studied incidentally by observing the damage around GEM holes after many discharges [41].

Figure 2.14 compares the spectra obtained from discharges in copper and aluminium GEM foils. In the case of the aluminium GEM, the peaks attributed previously to copper in Figure 2.13 are not visible. Instead, peaks that match aluminium emission lines are identified in the spectrum. Also, peaks attributed to the components of the gas mixture are present in both spectra. This further confirms that the method of identifying emission lines described in Section 2.2.4 is functioning correctly. Furthermore, the identification of the peaks attributed to the used GEM foil cladding material, in this case aluminium, is explained by its presence in the discharge plasma again pointing towards the vaporization of the material. When the two spectra are compared in terms of the intensity of the observed peaks, it can be seen that lines associated with aluminium are stronger than their copper counterpart. Although many processes and conditions are known to contribute to the final detected intensity of emission lines, this observation indicates more abundant presence of aluminium in discharge plasma. This can be supported by the vapor pressure curves of aluminium pointing to a higher vapor pressure for a given temperature compared to copper [42]. Therefore, at the same temperature, more aluminium is expected to be vaporized compared to copper. In first approximation, the reached temperatures of the GEM electrodes during a discharge should be similar for Al- and Cu-cladded GEMs when operated equally. This is because

## 2 Characterizing GEMs and THGEMs with different electrode materials

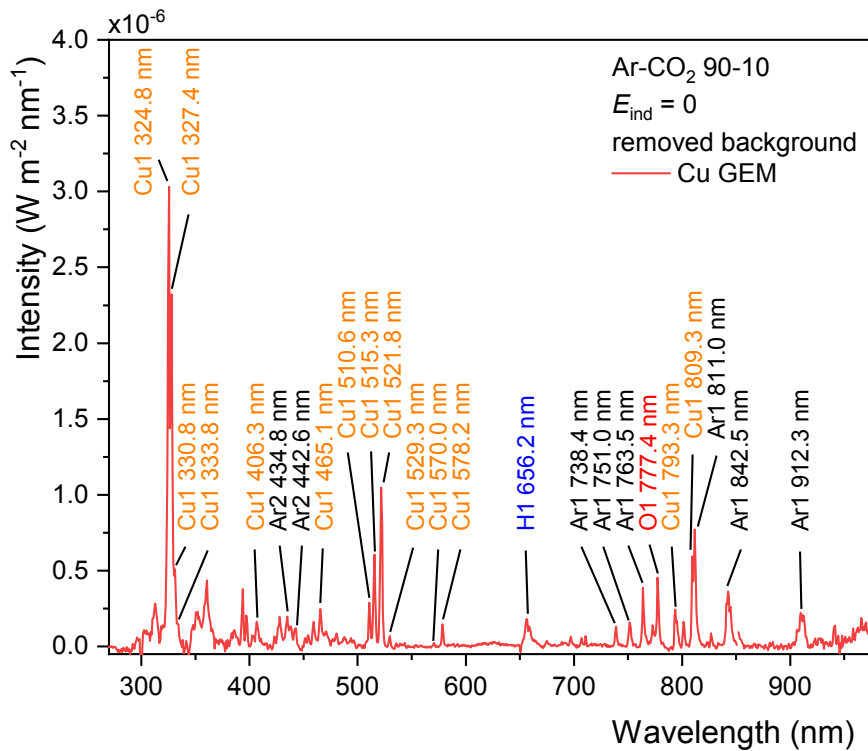


Figure 2.13: Emission spectra of primary spark discharges in copper GEM detector in Ar-CO<sub>2</sub> (90-10) mixture. Gas components and copper emission lines can be identified, the latter pointing to the vaporization of GEM foil material during a discharge.

both foils have a capacitance  $C$  of  $\sim 5.5$  nF. Considering a GEM foil as a capacitor, the electrostatic energy stored in the foil which is given with  $E = 0.5C\Delta V^2$ , which is released during the discharge process. However, during the measurements of the given spectra, the aluminium GEM was operated with a potential difference  $\Delta V$  of 420 V whereas the copper GEM is operated at 410 V. Therefore, the stored energy in the aluminium structure is  $\sim 5\%$  larger than in the copper one. This, and the lower thermal diffusivity, given in Table 2.1, of aluminium may result in slightly higher temperature of the aluminium surface reached in a discharge. This, together with the vapor pressure dependency on temperature, can explain observed relative intensities of the electrode material lines in the measured spectra.

However, without absolute normalisation of the element content in the discharge plasma and the calibration of the optical system for light absorption and reflection, it is not possible to extract the exact value of temperature with this method. As the material can vaporize, in principle, at any temperature, one cannot associate the observation of the material lines with any particular temperature value, e.g. melting point. Moreover, vapor pressure of aluminium at its melting point is almost four orders of magnitude lower than the corresponding value for copper [42]. The boiling point of the material, on the other hand, can provide an upper limit of the possible temperature range. It is therefore useful to study other materials and utilize this method as a temperature

gauge of the electrode region around discharging GEM holes.

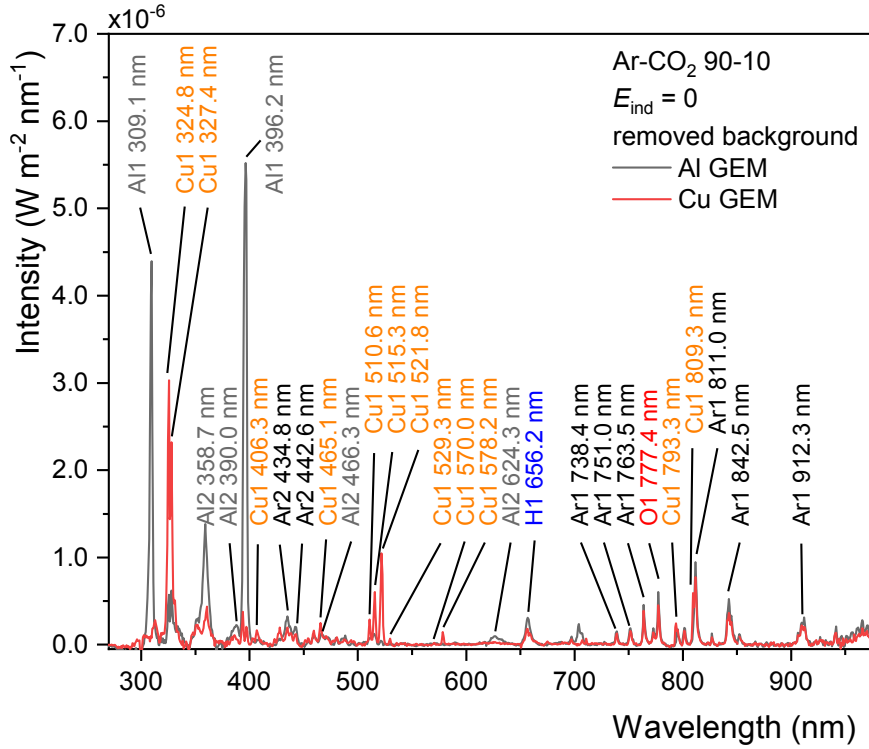


Figure 2.14: Comparison of emission spectra of primary spark discharges in copper and aluminium standard GEM foils. The emission peaks of the foil materials can be easily distinguished.

### THGEMs with different cladding materials

Fig. 2.15 presents the primary discharge light spectra of single-hole THGEMs with aluminium and copper electrodes are compared with the corresponding results obtained with GEMs. In contrast to what is shown in Section 2.3.1, no material lines are visible in the obtained THGEM spectra. A few small peaks in Al THGEM spectrum emerging around 356 nm and 396 nm might be associated with aluminium emission lines, but the expected peak structure from aluminium cannot be recognized. On the other hand, the gas constituent emission lines are well visible in both, GEM and THGEM, spectra. The absence of foil material lines in the THGEM spectra points towards significantly reduced material vaporization of the THGEM cladding layer. This points to the cladding material reaching much lower temperatures. Following the reasoning from Section 2.3.1, the absence of copper lines and hardly visible signals in aluminium THGEM spectrum indicate that the temperature of THGEM electrodes is most probably lower than  $\sim 2470^\circ$  (boiling point of aluminium). The capacitance of the THGEMs used in this study are at  $\sim 0.55$  nF and the potential difference at which the primary discharges are recorded is at  $\sim 1690$  V (see Section 2.3.2 and Table 2.2 for more details). Therefore, the energy stored in a single-hole THGEM discharge is at least 60% larger

## 2 Characterizing GEMs and THGEMs with different electrode materials

than in a standard GEM foil. Even so, the lower temperatures reached around the discharging THGEM hole can be explained by the thick cladding layer of a THGEM dissipating the heat more efficiently.

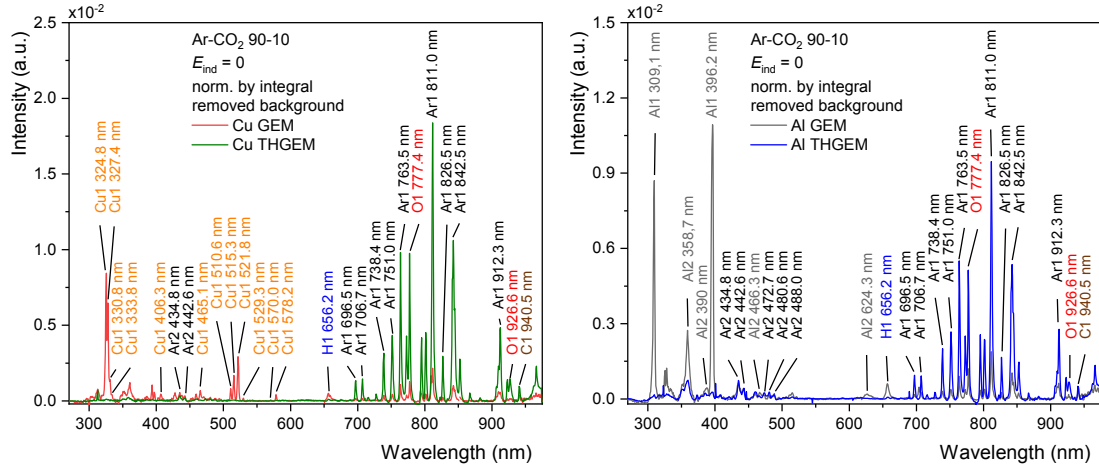


Figure 2.15: Comparison between GEM and single-hole THGEM primary spark discharge emission spectra obtained with copper (left) and aluminium (right) cladding.

As described in Section 2.2.1 multiple THGEMs incorporating different materials were produced. Figure 2.16 shows the spectra for all THGEMs, indicated in Table 2.1. Similar to the results observed with copper and aluminium single-hole THGEMs, none of the THGEM spectra exhibits emission lines corresponding to the material of the associated cladding layer. The only lines which can be identified are the emission lines of the gas mixture and contaminants. This points to the significant reduction of material vaporization in all of the studied THGEMs compared to GEMs. This observation is in agreement with the explanation that heat dissipated faster in THGEMs as all the used THGEMs have similar geometries.

### Emission spectra obtained with secondary discharges

In the last part of the spectroscopy measurements, light from secondary discharges is studied to determine how the two types of discharges differ in terms of their emission spectra.

Figure 2.17 shows how secondary discharges effect the emitted light spectrum in a tungsten THGEM as an example. The black line shown the spectrum from events with only primary discharges. The red line shows the spectrum of light emitted during events with primary and secondary discharges. This is because, as the secondary discharges can only be triggered by the primary sparks (see Section 2.1) it is not possible to exclusively capture the light from secondary discharges with the used long exposure method, described in Section 2.2.4. Instead, the light from events with an the induction field setting assuring 100% probability of the secondary discharge occurrence is analysed. It can still be recognized, that the addition of light emitted from secondary discharges does not considerably change the shape of the resulting

## 2 Characterizing GEMs and THGEMs with different electrode materials

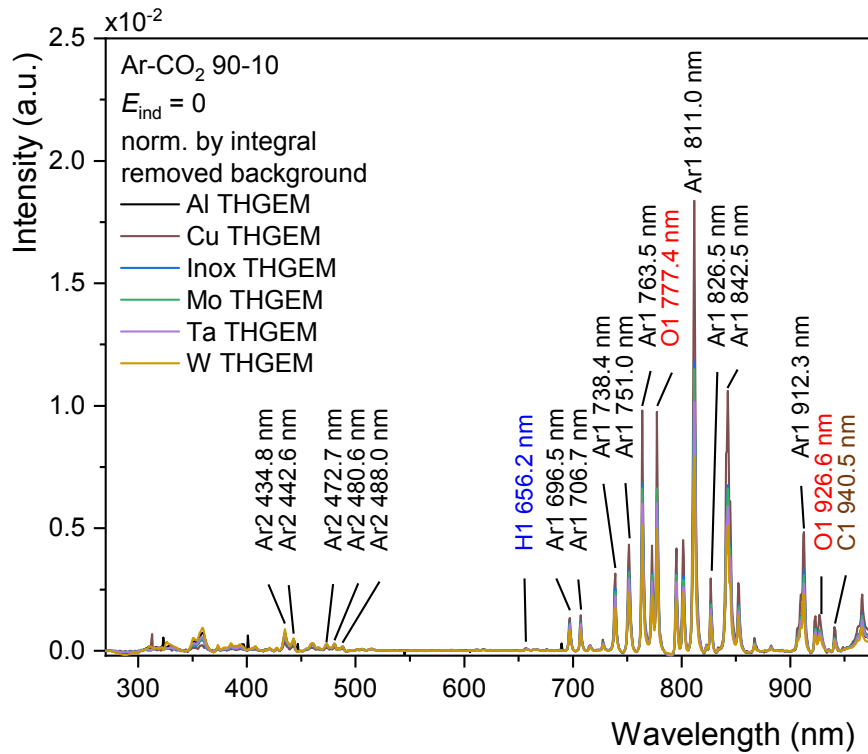


Figure 2.16: Emission spectra from primary spark discharges measured with single-hole THGEM foils with different cladding materials. No emission lines associated with the THGEM materials can be identified. All spectra share peaks attributed to the gas mixture.

spectrum. Importantly, no extra or new lines can be identified. Only the intensity of all visible lines is slightly increased with respect to the results obtained with primary discharges. This is expected as the spectra are normalized only to the number of primary discharge. This indicates there are no significant differences in light emission from primary and secondary discharges. In both cases, these are spark discharges, although their underlying triggering mechanism may still differ, which is discussed in Section 2.4.

It needs to be noted, that the secondary discharges can be triggered with all kinds of GEMs and THGEMs studied in this work (see also Section 2.3.2), independently from the cladding material. Although here tungsten THGEM is given as an example, the results obtained with different THGEM electrodes all lead to the same observation.

### 2.3.2 Material dependence in discharge formation

Next, the material dependency on the stability of the detectors against primary and secondary discharges is examined. Both primary and secondary discharge probability measurements have been conducted with all the GEM and single-hole THGEM structures introduced in Section 2.2. It shall be noted, however, that due to the defect developed in the aluminium GEM, comprehensive discharge studies of multi-hole GEM

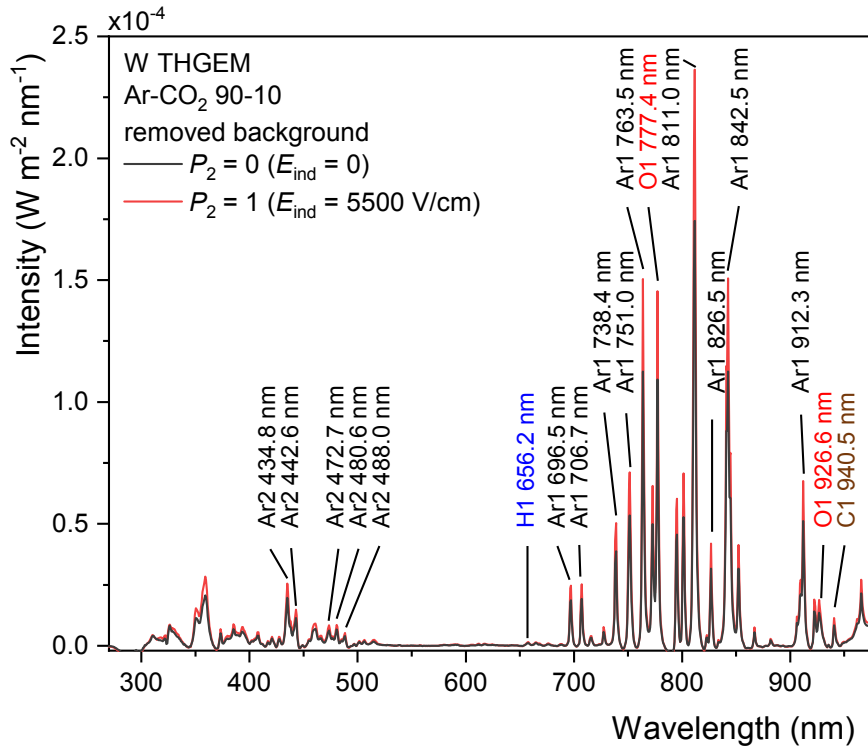


Figure 2.17: Comparison of emission spectra between events with only a primary spark discharge and events where both primary and secondary discharges are recorded, measured with the tungsten THGEM. Except for the variance in overall intensity, the shape and the peak structure of the spectra are identical.

structures have not been performed and will not be thoroughly presented.

### Primary discharge probability

First, the produced single-hole THGEMs are compared in terms of their stability against the formation of electrical discharges. Traditionally, the discharge stability is taken as a function of the gain, but due to the fact, that the gain evaluation of a single-hole structure is not possible with the employed setup, as described in Section 2.2.3, only an onset voltage for primary discharges is measured. The onset voltage is defined as the THGEM  $\Delta V$  at which the primary discharge rate reaches a value of  $\sim 0.2$  Hz, measured with 50% uncertainty. The results for all THGEMs are presented in Table 2.2. No significant difference is observed between the onset voltages measured for different cladding materials. Considering that the geometry of holes in all produced THGEMs are the same or very similar (see Section 2.2), the gain at the onset voltage of each structure is also expected to be similar. Thus, we conclude that there is no fundamental difference between the studied materials in terms of their influence on primary discharge stability.

This is well in line with the primary discharge formation mechanism, where the driving factor triggering streamer formation is the total number of charges collected in

## 2 Characterizing GEMs and THGEMs with different electrode materials

a single hole [4, 18]. Hence, with constant primary charge density as is the case in the conducted measurements, the probability of the streamer formation will depend on the hole geometry, not on the material of the electrode. Given the same hole geometry in all foils, no difference in their stability is expected. A potential influence of the material is foreseen for resistive electrodes, which may create a quenching mechanism by a local field reduction. However, the conductivity values of all electrodes studied in this work (see Table 2.1) are high enough to assume that the resulting resistance introduced in the circuit is negligible in comparison to the  $5\text{ M}\Omega$  protection resistor used in the setup (see Section 2.2.2).

Table 2.2: The operational limit for the used THGEM foils before the onset of primary discharges.

| Single-hole THGEM cladding material | Onset voltage of primary discharge formation (V) |
|-------------------------------------|--|
| Al                                  | 1690   |
| Cu                                  | 1680   |
| Mo                                  | 1700   |
| Inox                                | 1685   |
| Ta                                  | 1700   |
| W                                   | 1683   |

### Secondary discharge probability

The produced single-hole THGEMs were also compared in terms of their stability against the formation of secondary discharges. Figure 2.18 shows the secondary discharge probability  $P_2$  measured as a function of the induction field value for all single-hole THGEM foils. In addition a second copper THGEM sample is tested and presented in the figure, where their variance can be interpreted as a systematic uncertainty of the measurement. Also as reference, the secondary discharge probability of a standard copper GEM operated with the same gas mixture is given from [24]. It is however important to note that the effects of the hole and foil geometry on secondary discharge probability is not well established. Secondary discharges could be triggered with all of the structures, and reach 100% probability, at the fields where no amplification is expected, i.e. Townsend coefficient is zero.

## 2 Characterizing GEMs and THGEMs with different electrode materials

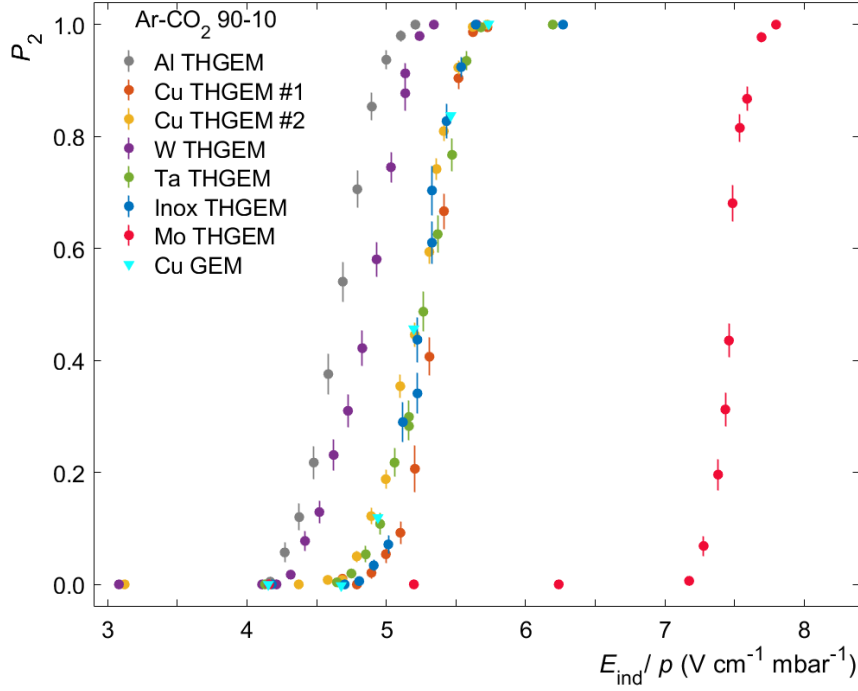


Figure 2.18: Secondary discharge probability as a function of the induction field measured with single-hole THGEMs with different coating materials. Field values are normalised to the ambient pressure of  $\sim 960$  mbar measured for each data sample.

Curves at higher induction fields in the given plot point to higher stability of the corresponding foil against secondary discharges. In contrast to the observations made with the primary sparks (see Section 2.3.2), clear differences can be observed between the secondary discharge probability curves obtained with different electrode materials. A group of similar curves can be identified around  $E_{\text{ind}} = 5 \text{ V cm}^{-1} \text{ mbar}^{-1}$  for copper, tantalum, steel THGEMs, and the reported standard GEM. For tungsten and aluminium, the secondary discharge curves are shifted towards lower fields, pointing to the reduced stability of such structures.

An especially significant difference can be observed for the molybdenum structure. The discharge curve is shifted towards much higher fields. Therefore it is shown, that the stability of a THGEM is substantially improved when using molybdenum electrodes. The reason for this is currently not explained and discussed in Section 2.4. Still, the use of molybdenum GEM and THGEMs is proposed a method to mitigate secondary discharges.

The obtained results with THGEMs can be compared to the measurements with standard copper GEMs in Ar-CO<sub>2</sub> (90-10) reported in [24] where the onset and slope of secondary discharge curves were measured at the induction field values between 5 and 6  $\text{V cm}^{-1} \text{ mbar}^{-1}$ , for different GEM foils. This shows that the variance in the onset fields between different samples of the same type may be as large as  $1 \text{ kV cm}^{-1}$ , comparable to the spread of secondary discharge curves observed in Fig. 2.18 for the

first six THGEM structures. On the other hand, it may point to the increased stability of standard copper GEMs (with the onset field of  $6 \text{ V cm}^{-1} \text{ mbar}^{-1}$ ) with respect to the aforementioned single-hole Cu THGEM.

### Time delay between primary and secondary discharges

In addition to the relation between the used electrode material and the secondary discharge stability, also the time delay ( $t_2$ ) between primary and secondary discharges is investigated, which is defined as the time difference between onsets of both signals measured at their steep, negative slopes. This is visualised schematically in Fig. 2.3. In Figure 2.19 the average time delays measured for all the used THGEMs are given as a function of the induction field and also the secondary discharge probability.

It can be observed that the measured time delay for different THGEMs are similar, starting from  $\sim 25 \mu\text{s}$  at lower discharge fields, reaching values below  $10 \mu\text{s}$  at high  $E_{\text{ind}}$ . The observed delay times are roughly compatible with the drift time of ions in the 2 mm induction gap. Also, the value of  $t_2$  decreasing with increasing induction field is in agreement with previous observations reported for copper GEMs in [24]. However, the dependency of  $t_2$  on the  $E_{\text{ind}}$  value cannot be explained by the corresponding dependency of ion mobility in Ar-CO<sub>2</sub> (90-10), reported in [43].

The only significant difference can be observed, again, for the the single-hole THGEM with molybdenum electrodes. Although  $t_2$  for the highest fields, at which secondary discharges are measured, is also  $\sim 10 \mu\text{s}$ , the time delay at lower fields is significantly longer. The difference is even more pronounced in the right panel of Fig. 2.19, where the time delay is plotted as a function of secondary discharge probability. At the intermediate  $E_{\text{ind}}$  field values, where  $P_2$  does not reach 100%, the time lag of the secondary discharge is roughly a factor of two higher than for all other THGEMs. This confirms the observation of distinctive properties of the Mo-coated THGEM.

## 2.4 Discussion

The main motivation of the presented work is to further study discharge formation mechanisms by employing amplification structures with different electrode materials. The results on primary spark development, where no correlation between the onset of primary discharges and the electrode material is observed, are in line with the well established streamer theory of spark discharge introduced in Section 2.1.2 [44, 45, 46, 47].

On the other hand, such a correlation with the used material, is clearly shown for the stability against secondary discharges in Figure 2.18. This feature does not comply with the streamer theory of a spark discharge. Together with the observed significant time lag of up to tens of microseconds, presented in Figure 2.19, it resembles the formation of a classic Townsend discharge [48]. On the other hand, it is argued, that the resulting discharge event observed in the gap below the GEM, is a spark discharge. The rapid development (see the scope signal in Fig. 2.3), accompanied by the acoustic signal indicate this. In addition, although this is not investigated in this thesis, it was shown in previous works [24, 22], that the secondary discharge formation highly depends on

the used gas composition. This mixture of different discharge signatures points to a more complex phenomenon. A mixture or a transition between Townsend (slow) and streamer (fast) discharge mechanisms might be the required for explaining these events. It is shown, that such transition mechanisms may appear at fields below the critical electric field [49]. In the case of a GEM-like structure, a secondary discharge process would be triggered by the Townsend avalanche, described with the Townsend first ionization coefficient, initiated by electrons from a primary discharge. Due to the lower than critical electric field in the gap, the secondary process being the development of a streamer is unlikely.

However, as shown in [24], the number of electrons stemming from a primary discharge with an energy high enough to ionize gas components (Ar, CO<sub>2</sub>) may reach a value of  $\sim 10^7$ . These electrons drift in the induction gap producing ions, which leads to the space charge accumulation close to the anode (here the readout electrode). The drift of charges in the induction gap was reported in [24] and can also be observed in Figure 2.19 where the measured time delay is in rough agreement with the expected ion drift time. Those drifting ions may cause secondary electron emission after reaching the cathode. In the presence of a strong field, it is possible that those emitted electrons. If a sufficiently high space charge is built up, the electric field distortions may eventually lead to local fields strong enough to achieve this, which might give rise to a streamer in the gap. This streamer would propagate towards the bottom GEM electrode. Therefore, the transition model discussed above complies fairly well with the observed signatures of secondary discharges.

However, the observed increase in time lag of secondary discharges measured with the molybdenum THGEM is puzzling. It is possible that the time necessary for space charge accumulation is longer as the number of secondary electrons extracted from the cathode is lower. This could also explain no secondary discharge development at lower induction fields, as one needs sufficient time and number of ions for a sufficiently large space charge build up. Only at the highest fields, exceeding the amplification field in a given gas mixture, the avalanche process is rapid enough to produce necessary amount of charges giving a rise to a streamer. This hypothesis, however, should be further investigated.

Coming back to the secondary emission of electrons, one proposed mechanism employs GEM electrodes heated by the primary discharge, which in turn facilitates the thermionic emission of further electrons upon ion bombardment and infra-red radiation [24]. In the studies described in this work, we do not observe a clear dependency of the secondary discharge creation on the temperature of the electrodes. On the contrary, we show that in case of THGEM electrodes, the temperatures reached upon a primary discharge are lower than for GEMs (see Section 2.3.1), whereas the onset field for the secondary discharge development remains the same, if not lower, as shown for Cu-based electrodes. In addition, differences between secondary discharge curves are not reflected in the emission light spectra discussed in Section 2.3.1. The intensity of the lines obtained with different THGEMs does not follow the same (or the opposite) order nor the identified lines differ between measurement with different materials.

This raises the question of whether the temperature effects are indeed crucial for understanding the mechanism of secondary discharge development. On the other hand,

we clearly see the dependence on the electrode material, reassuring that the secondary emission plays an essential role in these considerations. It is, however, surprising, that no correlation could be found with basic material parameters such as work function, which drives the emission of secondary electrons. The latter, however, highly depends on the quality of the metallic surface, including the possible creation of oxide layers, corrosion and operation under high temperatures [50] and should be studied in more details. Another hint towards this hypothesis may be the variance of onset fields for secondary discharges measured for different samples of copper GEMs and THGEMs (see Section 2.3.2), reaching  $1 \text{ kV cm}^{-1}$  or more [24]. The observed differences may be explained by the quality of electrode material. The available data is, however, too scarce to conclude whether the copper-based GEM is more stable than copper-based THGEM and whether the hole geometry and thickness of the copper layer have any influence on the secondary discharge development.

It should be noted, that the enhanced stability of the molybdenum THGEM could still be explained in a much simpler way. It may be, that the exceptionally good surface quality of the molybdenum electrode, especially around the rim, helps to avoid sharp metallic tips and edges which lead to high electric field values causing instabilities. The same argument could be, in principle, used for the observed higher stability (higher onset fields) of copper-based GEMs, reported in some measurements [24]. The quality of the edge of a chemically etched GEM hole shall be better than the drilled one. It is, however, not clear why measurements with different GEM samples yield different results. Following the argument in the previous paragraph, the onset field dependency on surface quality shall be systematically studied in order to make the final assessment of the observed variances. For the same reason, further studies are necessary to confirm the observations with the Molybdenum electrode, described in this work. Although the same results were obtained in several attempts, the studies should be repeated with an independently produced structure, including possibility of producing multi-hole molybdenum THGEM.

If confirmed, molybdenum electrodes may be a valid alternative for standard, copper-based GEMs, for the operation under extreme conditions. Note, the field values of  $\sim 7000 \text{ V/cm}$  are far beyond the usual settings at which GEM detectors are operated. However, employing molybdenum-based multi-hole (TH)GEM structures would allow one to apply extreme settings and operate the detector with highly-asymmetric fields around the foils. This could be beneficial for low ion backflow operation in, among the others, GEM-based photon detectors.

## 2 Characterizing GEMs and THGEMs with different electrode materials

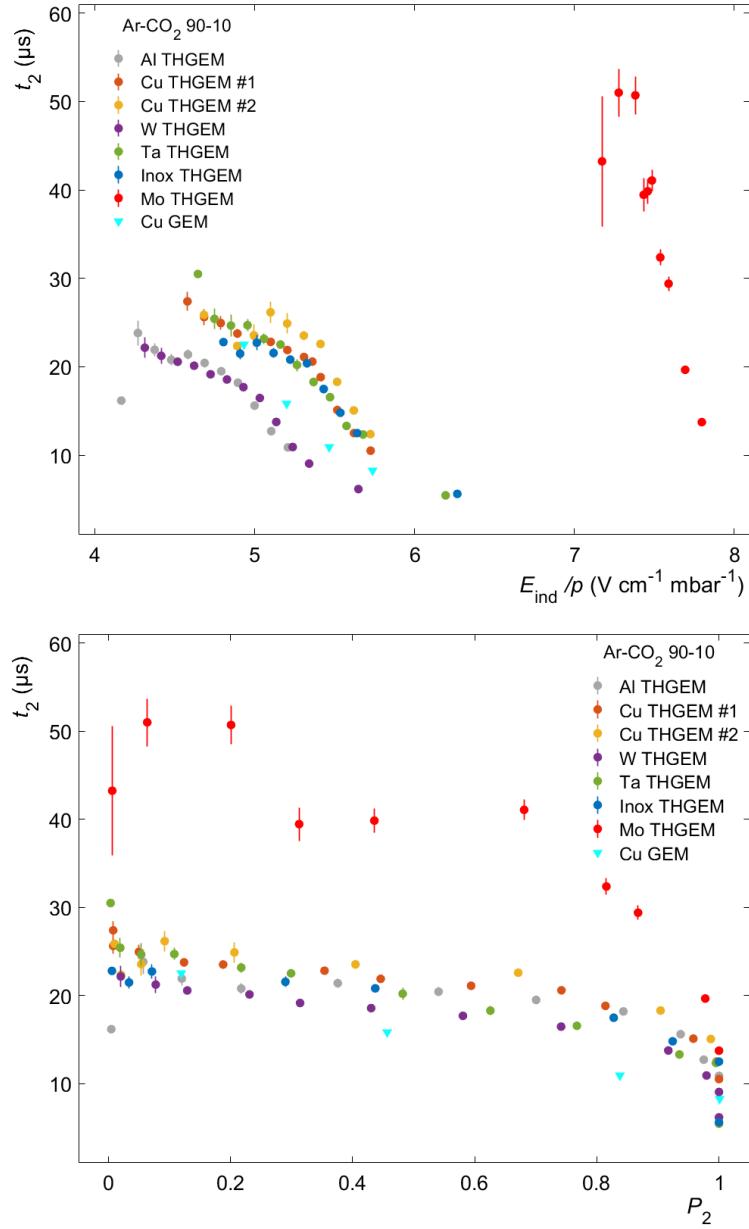


Figure 2.19: Average time delay between primary and secondary discharges as a function of normalized induction field (*top*) and secondary discharge probability (*bottom*). Error bars indicate the Standard deviation of the mean. The copper GEM points taken as reference from [24].

## 3 Development of a readout system for the RadMap telescope

The following chapter describes the development of a readout system based on the Padiwa front-end boards. This system was then used for the calibration and the qualification of a module produced for the RadMap telescope project. The Padiwa based readout system works on the principle of Time-over-Threshold (ToT), where the amplitude of the signal is not measured as with an Analog-to-Digital-Converter system but the time duration of the pulse over a set level is recorded. This approach yields some advantages such as good time resolution and practically infinite dynamic range. However, there are also some challenges associated with handling signals recorded using the ToT method, which are also discussed in this chapter.

### 3.1 The RadMap telescope project

The harsh radiation environment in space is a large obstacle in conducting safe human space missions. So much so, protection systems, such as shielded ship sections acting as radiation shelters are necessary for all vessels venturing beyond low-earth orbit. The type, energy, and direction of radiation are very variable with time and position, making it compulsory to also have monitoring systems. These would be especially needed to warn passengers during periods of high activity.

Such monitoring systems are normally either wearable personal dosimeters that are compact, light and have low power consumption, or area monitoring detectors that are capable of characterizing the local radiation environment comprehensively. Wearable devices so far have mainly been passive dosimeters measuring the total ionizing dose the wearer is exposed to. As they are only read out once back on earth, these devices are not capable of real-time dose rate monitoring. Also, the linear energy transfer (LET), the energy individual particles deposit in the sensor, cannot be measured with passive dosimeters. LET is a critical measure for determining the biological effects expected by radiation exposure. Recently developed active dosimeters can provide these capabilities to a certain extent. Still, they too are lacking in terms of determining the angular distribution of the radiation. As such, this task is traditionally handled by bulkier and power-hungry area monitoring systems, which are installed in certain positions of the vessel. Usually composed of many different types of detector technologies, these monitoring systems are capable of determining the incident direction and the kinetic energy of ambient radiation. Even so, current particle telescopes used in area monitoring are limited in terms of their field of view.

### 3 Development of a readout system for the RadMap telescope

The RadMap telescope project aims to deploy a proof-of-concept radiation monitoring telescope to the International Space Station in 2021 [2]. The telescope has a very compact design (10 cm × 10 cm × 10 cm size, <3.5 kg weight) and low power consumption (30 W), enabling it to be used as a wearable radiation monitoring system. It combines many capabilities of different particle detectors currently used in space such as the online measurement of the dose rate, LET and particle-dependent energy spectrum. Moreover, it is capable of tracking charged particles with omnidirectional acceptance overcoming the field-of-view limitations of other telescopes. Although there are specialized devices with better performance in these single categories, the RadMap telescope combines multiple measurement capabilities in one compact device. Making it possible to reduce the number of different radiation monitoring devices required in a vessel.



Figure 3.1: Rendering of a fully assembled RadMap telescope [2].



Figure 3.2: The RadMap module used in the studies.

The full telescope contains five radiation sensors. These include two experimental scintillator dosimeters as well as two flight-proven silicon dosimeters providing total ionizing dose and online dose rate measurements. The last detector is the Active Detection Unit (ADU) which is the main sensor of the RadMap telescope. The omnidirectional particle tracking and energy determination capabilities of the RadMap telescope discussed earlier is achieved by the ADU. It detects particles by the emitted scintillation light when particles go through the 1024 plastic scintillating fibers in its active area. The full ADU consists of 4 identical sub-modules, each incorporating 8 layers of 32 scintillating fibers. The emitted light from the fibers is read out by silicon

photomultipliers (SiPM). The SiPMs are placed on 4 PCBs, one on each side of the module. A photograph of a single ADU module is shown in Figure 3.2. The power and the data links to the SiPMs are placed on the PCBs. In total twelve samples of such modules were produced. Four to be assembled in the final telescope to be deployed in ISS, four as flight backup spares and four additional spares for further tests and studies. In the measurements conducted in this thesis, one of the modules belonging to the last category is used and studied.

### 3.1.1 Scintillating fibers

The modules making up the ADU consist of 256 scintillating plastic fibers. Produced by Kuraray with a model number of SCSF-78 [51], these fibers have a length of 80 mm and a square cross-section of  $2\text{ mm} \times 2\text{ mm}$ . The used fibers have a peak emission at 450 nm and a decay time of 2.8 ns. A picture of a bunch of the fibers before they were bonded into modules is given in Figure 3.3. The fibers are positioned in each module in 8 layers in an alternating horizontal and vertical direction. Moreover, fibers on parallel layers are placed staggered at a distance of half fiber thickness. This is done to minimize the dead zone introduced by the cladding layers or by air gaps. The module geometry is shown in Figure 3.4



Figure 3.3: Photograph of a fiber bunch before being installed into the modules.

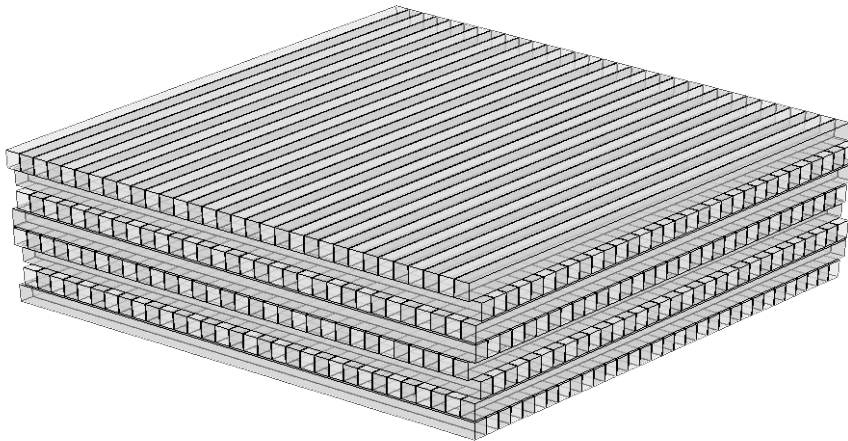


Figure 3.4: Representation of the fiber layout geometry .

The fibers consist of a polystyrene scintillating core surrounded by a PMMA (Poly methyl methacrylate) cladding layer with a thickness of 2% of the entire fiber ( $20\text{ }\mu\text{m}$  cladding on each side). The cladding is important not only for protecting the fiber from

mechanical surface abrasion but also for transporting the emitted scintillation light to the readout SiPMs. This is achieved by total reflection in the interface between the fiber core and cladding layer as shown in Figure 3.5. As such, all sides of the fibers but the one facing the SiPMs is cladded to achieve maximum light collection. The scintillation process inside the fibers is driven by the excitations of the free valence electrons of the molecules by incident radiation [52, 53].

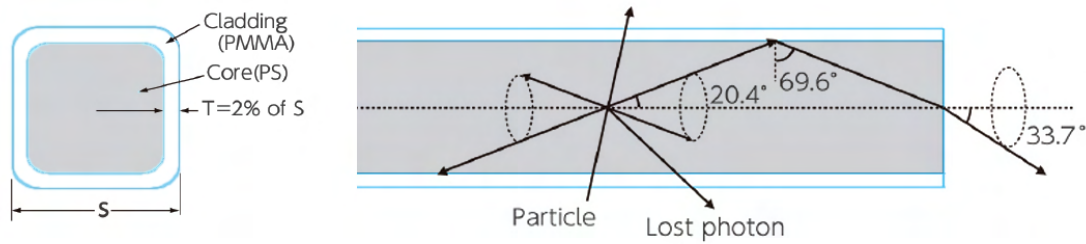


Figure 3.5: (left) Sketch depicting the cross section of the used scintillating plastic fibers. (right) Representation of the total reflection process utilized in transporting the scintillation light towards the readout.

### 3.1.2 Silicon Photomultipliers

The collection and the readout of the emitted scintillation light are achieved by utilizing Silicon Photomultipliers. SiPMs are silicon-based solid-state low-level light sensors. They consist of an array of silicon avalanche photodiodes (APDs). To achieve high gain, the APDs are operated in Geiger-mode, meaning that incident photons lead to an electric breakdown in the APD structure. Thus, with such an operation, each of the APDs generates binary output. A SiPM consists of many APD cells (in the order of hundreds to tens of thousands), which are connected to a parallel common cathode and anode output. With this, the output signal from the SiPM is the superposition of all the micro APD cells, which is then a signal proportional to the input light intensity. In Figure 3.6 a sketch of the micro-cell structure of a SiPM and a photo of one of the SiPM arrays used in the RadMap modules can be observed.

### 3 Development of a readout system for the RadMap telescope

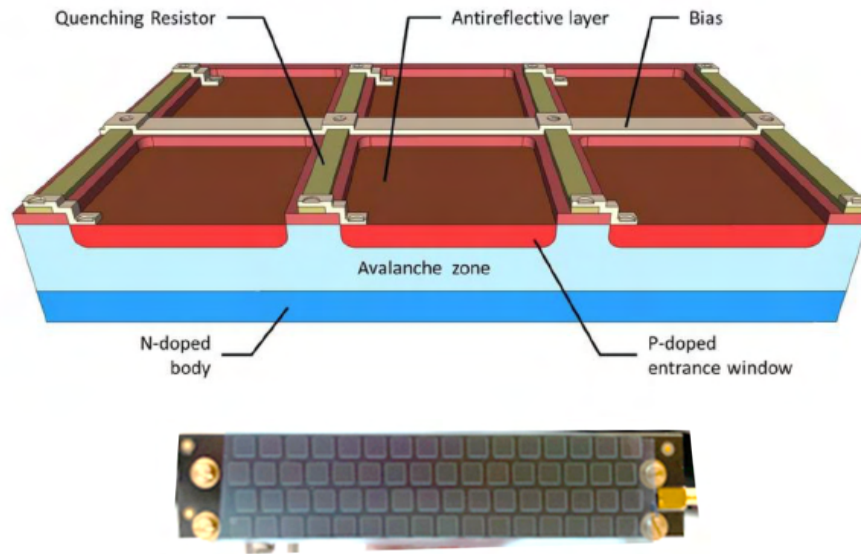


Figure 3.6: (top) Sketch depicting a cross section of a SiPM consisting of an array of microcells. Each microcell acts as a micro APD operated in Geiger-Mode and are connected to one another. (bottom) Photo of the SiPM configuration used in the RadMap modules.

For the ADU modules of the RadMap telescope, SiPMs of model PM3325-WB-D0 from the company Ketek are utilized [54]. They have an active area of a  $3\text{ mm} \times 3\text{ mm}$  with 13920 microcells of  $25\text{ }\mu\text{m}$  dimension. The breakdown voltage lies between 24 V to 25 V depending on the temperature and they are operated at an applied voltage of 29 V corresponding to an over-voltage of 5 V. In Figure 3.7 signals from a positive polarity SiPM recorded with an oscilloscope is shown. It is possible to recognize how changing the over-voltage increases the output pulse amplitude for the same input. To optimise the detection efficiency, the used SiPMs are chosen to be the most sensitive for the light which closely matches the peak-emission wavelength of the used fibers.

### 3 Development of a readout system for the RadMap telescope

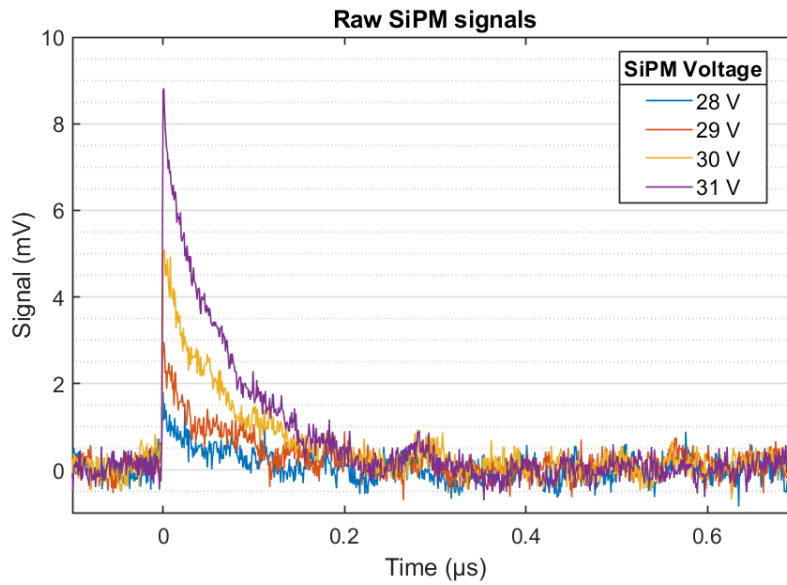


Figure 3.7: The raw signal output from a single SiPM operated at different applied over-voltages. In all cases the SiPM is illuminated with a very faint constant light source from the LED flasher (ats4=75 with filter).

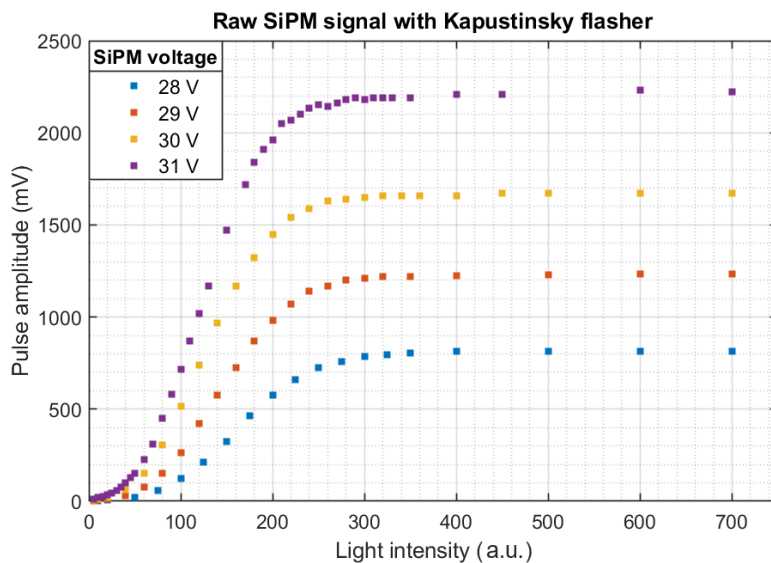


Figure 3.8: The amplitude of the raw signal output from a single SiPM illuminated with a LED flasher as a function of the intensity setting of the flasher. The saturation curves for different applied SiPM voltages can be observed.

Another property of SiPMs is the fact that their signal output saturates with increasing input light intensity, due to the limited number of microcells making up the sensor. Once triggered the microcells provides a binary hit signal not proportional to the number of received photons. As such, the signal from light intensities high enough to

trigger all microcells are indistinguishable. Approaching the saturation limit, the linear response of the sensor is lost. This can be observed in Figure 3.8. The non-linear trend for low light intensities seen in the plot is explained by the non-linear performance of the used LED flasher.

## 3.2 Development of the readout system

Towards the goal of particle detection, multiple steps and apparatus are required. In the previous section, it was introduced how the RadMap telescope utilizes plastic scintillating fibers to convert the energy deposited by radiation into photons which in turn is converted to an electronic signal with SiPMs. Still, one more critical step is required before the particle information is acquired in a form enabling its processing and analysis. This is the digitization of the analog signals from the SiPM and is the task of the readout system. In the case of the RadMap telescope, the readout electronics utilizes the IDE3380 application-specific integrated circuit developed by Integrated Detector Electronics AS for use with solid-state photodetectors. This chip works on the principle of Analog-to-Digital Converters (ADC), Where an additional Field-Programmable-Gate-Array (FPGA) system handles the data stream of the digital signals from the IDE3380 while also building events by applying cuts and trigger conditions. Afterwards, the event data is sent to the central control unit housing the computer where the data is finally stored or transmitted back to the ground via a downlink. Using this arrangement, the telescope achieves a total power consumption of around 30 W. Moreover, with the used 16:1 multiplexed ADC system, the telescope setup has the capability of recording event rates of up to 6.5 kHz which well exceeds the rates expected during operation in the ISS. In future applications such as radiation monitoring during interplanetary journeys, a higher rate performance is expected to be required. To this point, utilizing Time-over-Threshold (ToT) based readout systems, which are capable of fully parallel recording of all channels, is a good candidate.

### 3.2.1 ToT based Padiwa+TRB3 readout electronics

The Padiwa+TRB3 readout system, initially developed at GSI for the HADES experiment and used in the CBM RICH, utilizes the ToT method for reading out signals from photodetectors [55, 56, 57]. Shortly, the Padiwa front-end cards are capable of converting the analog input signal from 16 channels to time signals in form of Low-Voltage-Differential-Signals (LVDS). These signals are in turn registered with the Time-to-Digital converters (TDC) on the TRB3. The full readout is achieved in multiple steps.

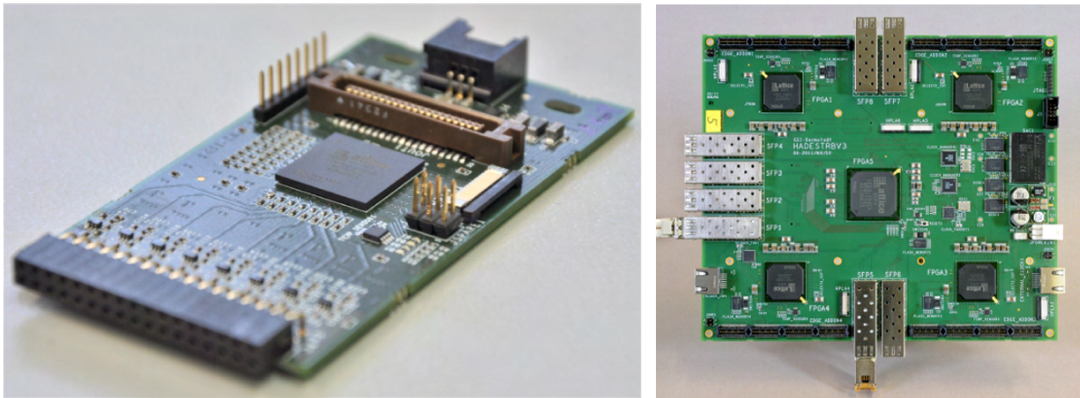


Figure 3.9: (left) The Padiwa front end card responsible of converting the input signals from the SiPMs to time signals. (right) The TRB3 system housing the Time-to-Digital converters and the Central-Trigger-System for operating all the connected Padiwas.

The Padiwa cards offer a 16 channel 2 mm pin-head connector, where the analog signal from the photo-detector is connected. The input signal is initially amplified (with a gain of 10) and then attenuated. The attenuation step cuts high voltage pulses in the system reducing noise and crosstalk. It is important to note here that the attenuation does not disturb the signal measurement, as the signal amplitude is not directly probed with the ToT method. Next, an integrator circuit is used on all channels reducing noise after which all channels are connected to an FPGA. A threshold with adjustable voltage level is set via Pulse-width-Modulation with a threshold circuit in the FPGA utilizing wide-band amplifiers and RC low-pass filters. With the threshold level set, the FPGA generates a time signal, with the discriminator circuit it features, from the comparison between the analog signal and the set threshold. With this, the resulting output signal from the Padiwa for each channel is an LVDS time signal proportional to the Time-Over-Threshold of the input signal. The LVDS is a commonly employed signaling standard excelling in reducing noise [58]. The output LVDS is connected to an IDC (insulation-displacement contact) connector to which a cable is plugged for transmitting the signal to the TRB3.

The TRB3 is a data acquisition system suitable for use in a wide range of applications [55]. Designed according to the COME & KISS concept (COMplex COMmercial Elements & Keep It Small and Simple) it houses five Lattice ECP3-150EA FPGAs, four of which are configured as TDCs with  $<20$  ps root-mean-square (RMS) time precision between two channels and 256 signal channels in total. During operation the TDCs record the leading-edge timestamp and the ToT information of hits, where channels can save up to 127 hits per event. A central FPGA provides the Central Triggering System (CTS) used for controlling the data taking. It provides calibration triggers to the TDCs and event triggers which separate the measurement into time frames called CTS events. The interface between the TRB3 and user is achieved via a desktop computer over a LAN connection. The run parameters can be configured using a CTS web interface and the data acquisition is controlled via the Data Acquisition Backbone Core (DABC)

framework [59]. Finally, the recorded data is accessed and analysed using the ROOT Data Analysis Framework [60].

### 3.2.2 System preparation and tests

For the operation of the Padiwa+TRB3 readout system with the modules from the RadMap telescope, adapter PCBs were produced to interface the two systems. Moreover, tests were conducted to determine the optimal operational methods of the assembled system and to characterize its performance.

#### Production of adapter boards

To connect the readout system to the RadMap modules, an adapter board is required. The main purpose of the adapter board is to enable connecting the different types of connectors used on the two systems. Furthermore, the signal transmission of the 64 channels from the SiPM-boards had to be separated to be read out with the 16 channel Padiwa front-end card. The mapping is configured in such a way that each of the Padiwas reads out channels corresponding to half the fibers in one layer of the module. With this, it is possible to decide which layers of the module are to be read if there are not enough Padiwa cards for a full 256 channel readout. Figure 3.10 depicts the final version of the produced adapter board. The design of the PCB layout according to the provided schematics and mapping is done at the ZEL Electronics Group at TUM [61]. In addition to the signal transmission, the board also houses a connector for powering the Padiwas.

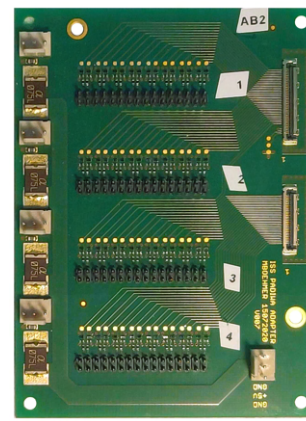


Figure 3.10: Adapter board between the RadMap module and the Padiwa front-end cards.

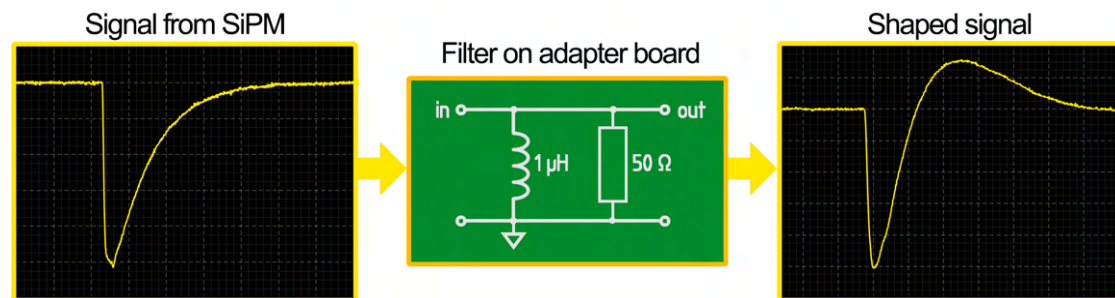


Figure 3.11: Schematic depicting the filtering applied to the signals. The raw signal from the SiPM (*left*) is shaped on the adapter board with the given filter design. The output signal has a overshoot following the initial peak, which ensures that the signal will promptly go under threshold also with added noise.

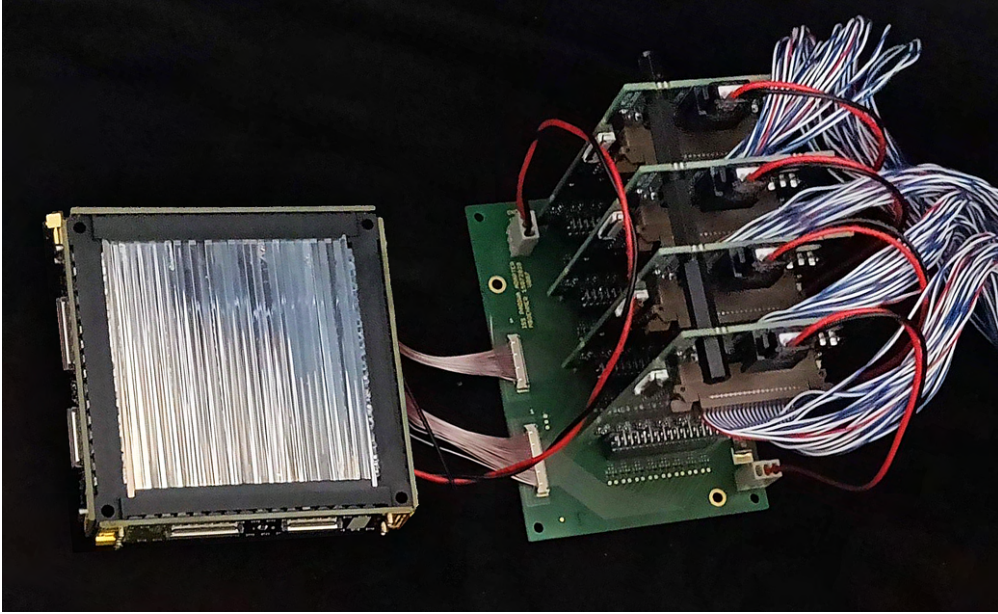


Figure 3.12: The RadMap module connected to four Padiwas via the produced custom adapter board. In the shown configuration, one of the four Ketek boards (64 channels, every second fiber in horizontal direction) on the module can be fully read out.

Finally, the adapter board incorporates a signal filter on each signal channel. The filtering, as depicted in Figure 3.11, is designed to smoothen the saw-tooth like pulse from the SiPM and to add oscillation. This shaping is done to mitigate errors in the ToT based readout process introduced by environmental electromagnetic interference (EMI). This is especially important for signals expected when detecting minimum ionizing particles (MIPs), which lead to weak pulses (amplitude of 5 mV to 20 mV). Optimal filter parameters, such as the used inductance value, depend on the used signal chain. Therefore, multiple values were tested and compared with the readout system. Among the investigated values, it is observed that the  $1\ \mu\text{H}$  and  $50\ \Omega$  filter design, depicted in Figure 3.11 leads to the best efficiency of registering small signals. This is tested by applying very faint light using an LED flasher to a single SiPM and comparing which filters lead to the best detection efficiency. The produced adapter boards were populated with inductors and resistors according to the obtained parameters.

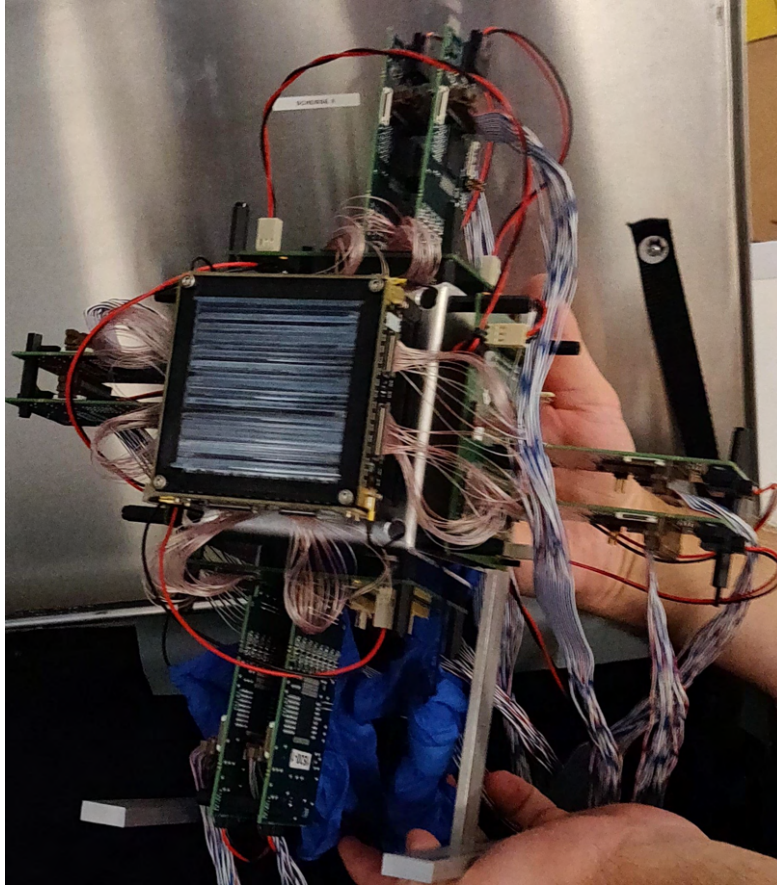


Figure 3.13: The setup used in the test beam. The RadMap module with the scintillating fibers can be seen in the middle. Around it, two Padiwa cards are mounted on each of the four adapter boards. The detector was housed in a light tight box during operation.

### Noise and crosstalk analysis

Due to the small signals expected during operation of the tracker for measuring MIPs (cosmic muons or pions in the test beam), it is especially important to quantify the noise in the system. It is observed that the EMI conditions in the lab can lead to fake hits introduced by the noise. By increasing the threshold level configured in the Padiwa FPGA, it is possible to mitigate fake hits. However, this in turn reduces the detector efficiency where signals from particles traversing small lengths inside the fibers are no longer recorded. The threshold level can be adjusted in steps of  $50.35 \mu\text{V}$ . The analysis of the recorded fake hit rates reveals, that these lead to small ToT values. This is explained by the high-frequency component of the EMI noise leading to short signals over threshold. With this, it is decided that a fake hit rate below 1 Hz is acceptable for operation. This is determined to be true for a set threshold of 5.35 mV (or 100 steps) in lab conditions. As such, the tracker is operated with a threshold setting of 100 in the presented studies. However, during the beam test discussed in Section 3.3, it is observed that a higher rate of fake hits is recorded in the beam cavern tests than in lab

conditions. Still, this noise is removed in post-processing by applying a cut on the ToT distribution of the recorded signals.

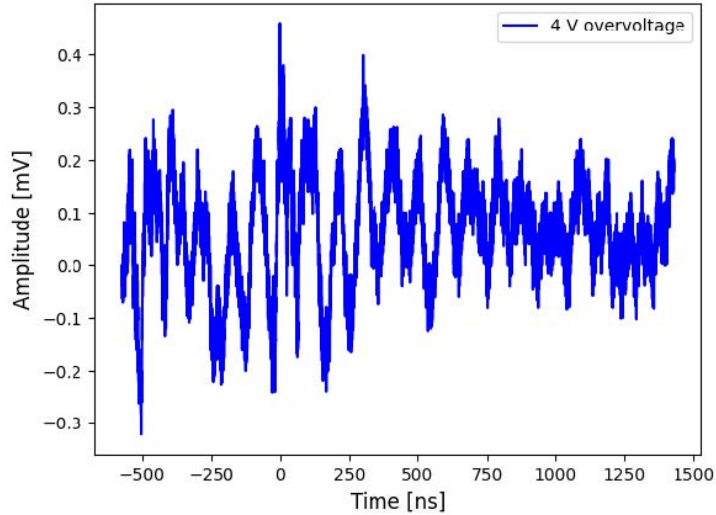


Figure 3.14: The noise recorded on one of the signal channels from the SiPM in dark conditions with an oscilloscope. With the Padiwa readout system connected, the observed noise is expected to be significantly higher due to the amplifiers with a gain of factor 10.

With the set threshold level, when large signals (over 50 mV) are being read out, induced for example by protons crossing the module, the oscillations following the initial pulse can also lead to fake hits. Surprisingly, it is shown that although the oscillations have lower amplitude than the original pulse, they lead to higher ToT values. Figure 3.15 depicts a signal which leads to such an observation. As such, these unwanted hits cannot be removed from the data simply by cuts on the ToT distribution without significantly limiting the dynamic range of the detector. Still, using the timestamp information recorded for all the hits, a post-processing cut is introduced which rejects follow up hits on channels, taking only the first hit for each event.

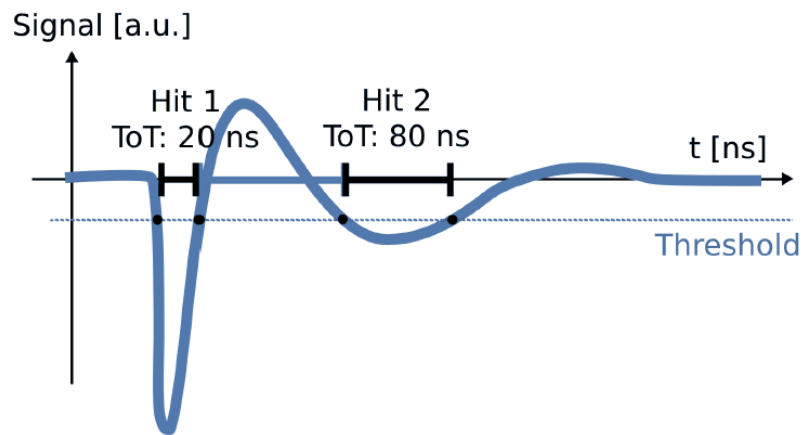


Figure 3.15: How the oscillations of the signal lead to multiple hits with varying magnitudes when measured with the ToT method.

Finally, the crosstalk between the channels of the detector is investigated, which has two possible origins. First, the electrical crosstalk between adjacent signal channels in used cables and PCBs. Second, optical crosstalk between the fibers and SiPMs inside the module. The electrical crosstalk is tested by applying signals of varying amplitude to single channels of the readout scheme and monitoring the hits recorded on adjacent channels. The signal for these tests originates from a single SiPM flashed periodically with an adjustable LED light source. It is determined that with the used readout scheme and the described threshold setting, signals below 100 mV do not lead to hits on adjacent channels. This is well above the signal strengths expected from the module while measuring MIPs during the beam test, and as such electrical crosstalk is not expected to be observed during the measurement campaign. On the other hand, since it is not possible to isolate individual fibers inside the used module, the direct characterization of the optical crosstalk is not possible. Instead, the optical crosstalk is probed in data measured during the beam test.

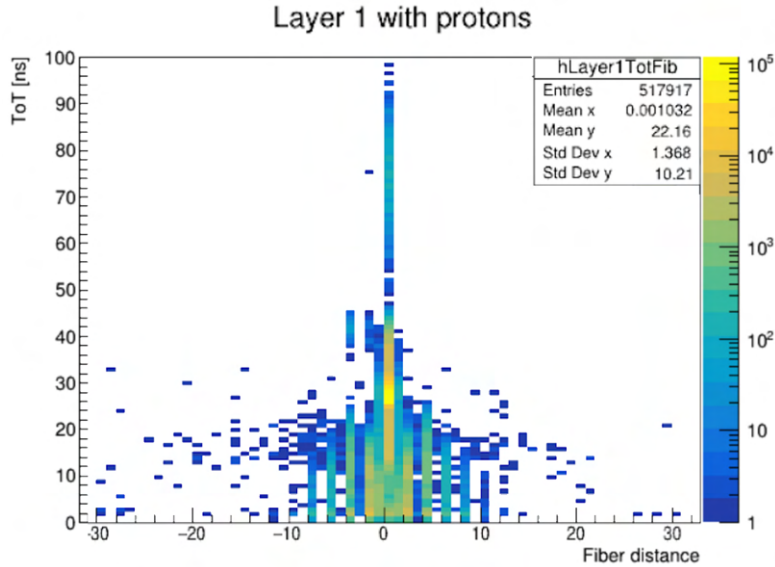


Figure 3.16: The distribution of recorded proton hits on Layer 1 of the module plotted as a function of the measured ToT and the relative position to the first hit in the same event.

Figure 3.16 depicts the signals recorded on Layer 1 during the beam test campaign described in Section 3.3 as a function of the ToT value of each signal and its relative distance to the first hit on the corresponding layer within the same event. As there is no cut on multiplicity in the given plot it can be observed that most recorded hits lie in the bin corresponding to zero fiber distance meaning that most events have only a single hit. Still, it is possible to recognize hits with larger than zero distances, where these can be associated either with fake hits due to optical crosstalk or particles going through multiple neighbouring fibers. The module is designed in such a way that the fibers are coupled to a SiPM on alternating sides. Especially these fibers, which are separated by factors of two appear to have many common signals in the given distribution. It is expected that optical crosstalk can only occur in the region between fibers and SiPM. Therefore, the hits observed observed in plot, complying with this, are explained to have been introduced due to optical crosstalk. Repeating the same analysis with pions, this pattern is not observed. Accordingly, it is concluded that the light generated in pion events is not strong enough to lead to fake hits being registered on neighbouring SiPMs due to crosstalk. In conclusion, optical crosstalk is not expected to significantly alter the performance of the detector when measuring MIPs.

### Time calibration

The recorded time information of hits on all channels must be properly tuned. This is especially important for tracking of particles with high rates. In the assembled system, the main source of varying time delays between the channels originates inside the FPGA of the TRB3. This is due to the different propagation durations of the signal on different channels during the TDC process. For the characterization of the relative delays between channels, time calibration measurements were conducted. For this, the

signal from a single SiPM flashed periodically with an LED is sent to 8 Padiwa inputs simultaneously using a fan-out cable. The measurement setup is depicted in Figure 3.17. Due to the limit that only 8 channels can be compared with a single measurement, the process is repeated by connecting the pulser to different positions until all channels are tested.



Figure 3.17: Sketch depicting the setup for measuring the relative time delays between channels for time calibration.

For obtaining the calibration factors, first the timestamp information of hits on all the channels are recorded. One channel is chosen arbitrarily as the baseline and the time difference between all channels and the baseline is calculated. The resulting distributions are then fit with a Gaussian distribution and the mean is taken as the time delay value. Figure 3.18 shows the time delays between the channels on each TDC on the TRB3. As can be recognized, the pattern is similar on all TDCs which are run via the same firmware on four FPGAs. Using this, the final calibration values are taken as the average of the measured time differences of the same numbered channels on all TDCs. With these values determined, the time calibration is applied by subtracting them from the timestamps of all recorded hits in the corresponding channels. The time calibration between the different TDCs is done by using a reference channel present on each TDC, which all simultaneously receive a signal from the central triggering system on the TRB3 at the beginning of each event period.

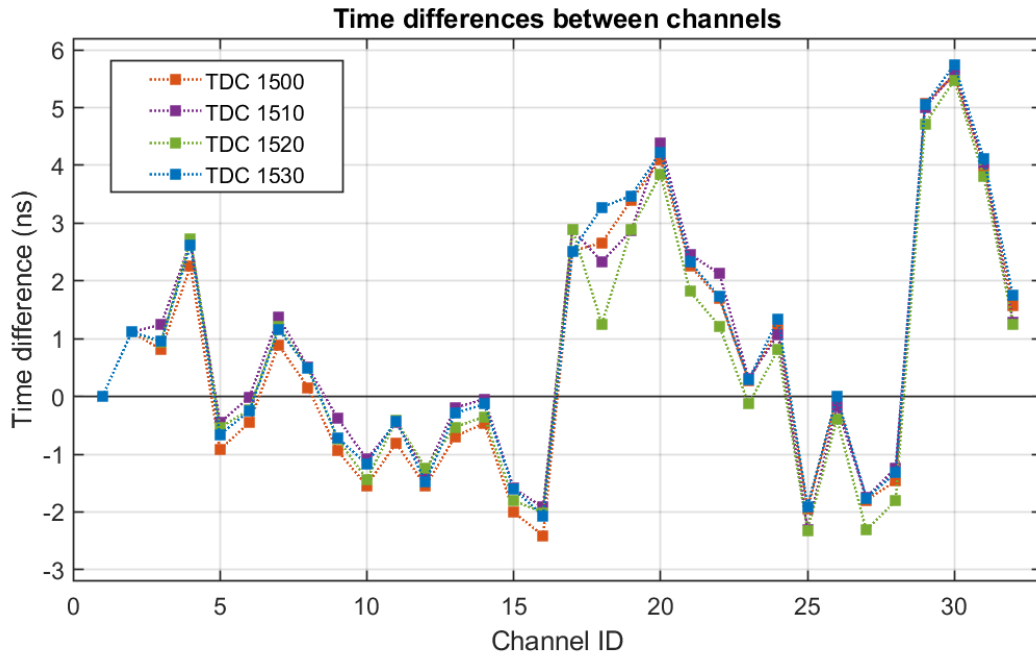


Figure 3.18: The difference in measured hit timestamp between different channels when a signal is sent simultaneously to all. Due to the different propagation times for all channels inside the FPGAs on the TRB3, different channels have different delays. The same delay pattern can be recognized in all TDC registers which have the same FPGA configurations.

Figure 3.19 presents the comparison of the measured time calibration values with the time delays between recorded hits in the beam test. The latter analysis is done in a configuration where the beam is parallel to the module surface. This means that particles go through all fibers of a single layer. Considering that the pions from the beam traverse the entire module in 300 ps, it is assumed in the calculations that all the hits occur simultaneously as with the measurements conducted in the lab. The resulting relative time differences between the channels from this method are in good agreement with the determined time calibration values. As a result, by implementing the time calibration in post-processing, the overall time resolution of the tracker is brought down from  $\sim 15$  ns to  $\sim 3$  ns.

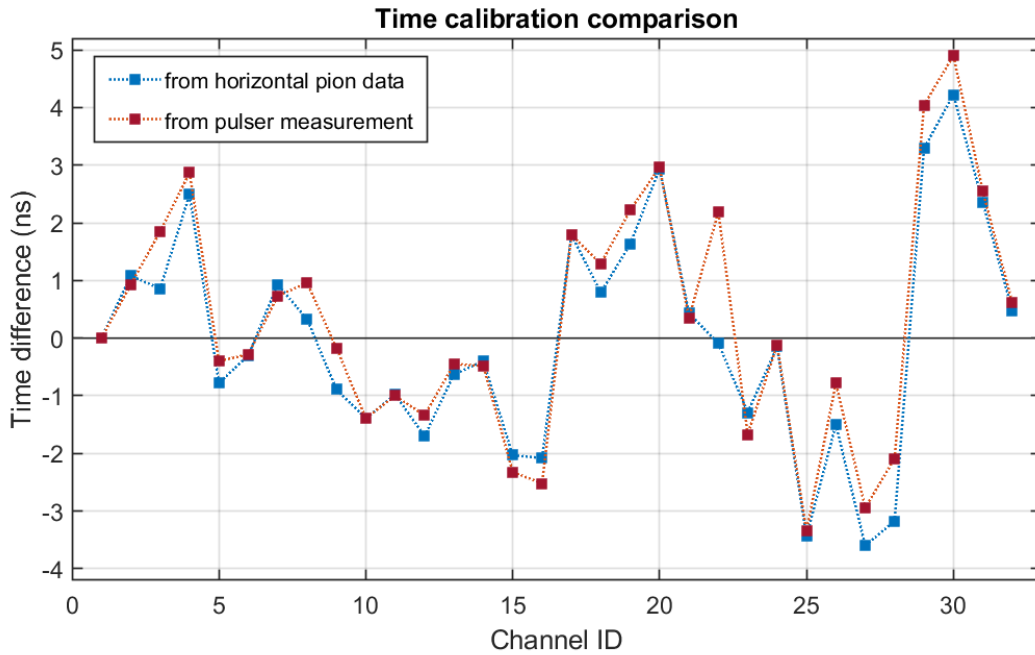


Figure 3.19: Comparing the obtained time calibration values using the pulser setup with the time differences observed in the beam time in a configuration where pions go through all the fibers in a single layer.

### Padiwa gain calibration

Similar to the timestamp information, also the ToT values of the recorded signals from different channels can show variances and should be corrected. To alleviate variances introduced inside the TRB3, an internal calibration pulser is used for the ToT calibration of the TDCs. This is achieved by sending 30 ns long gate square wave pulses to all of the TDC channels, and forcing the mean of the recorded ToT distributions to the expected 30 ns value. Still, it is shown that other sources of variances exist throughout the readout chain. This can be seen in Figure 3.20, which depicts the ToT distributions of signals recorded from a single SiPM connected directly to Padiwa channels. The SiPM is flashed with an LED light source in the same configuration as in Section 3.2.2 and the internal TDC calibration is applied. Here, the peak, which lies on most channels at a ToT value of  $\sim 15$  ns, is associated with the signals from the single SiPM. However, it is clear, especially when Padiwas corresponding to Layer 2 are examined (top-right plot), that not all channels respond the same way to the same signal.

This variation comes from the differences in the amplification on all the channels on the Padiwas. As introduced in Section 3.2, all channels of the Padiwa utilize fast-amplifiers as the first step of the signal handling. The gain of these lie on average at a factor of 10, however the variance between channels on different Padiwas is observed to be rather large leading to differences in ToT measurements. Especially the zigzag pattern observed in Layer 2 is determined to be due to one of the used Padiwas, reading out the even numbered fibers on Layer 2, having amplifiers with

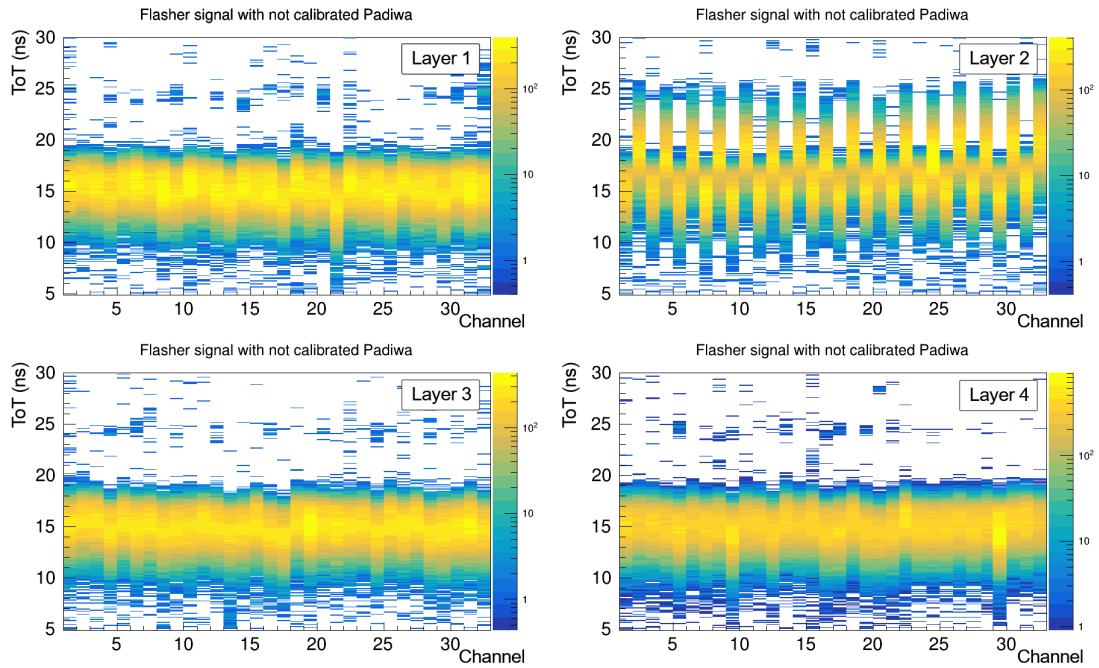


Figure 3.20: The ToT distribution of signals recorded with Padiwas connected to a single SiPM flashed with an LED light source.

higher gain than the others. To alleviate the variations introduced by the Padiwas a gain calibration is conducted. As the ToT procedure strongly depends on the signal shape, a ToT calibration measurement should be conducted with signals of the same shape as expected during operation. A stand-alone signal generator capable of delivering the fast pulses of SiPMs was not available during the tests, hence a single SiPM flashed with an LED light source is utilized as the signal source. The used measurement setup is similar to the one used in the time calibration measurement shown in Figure 3.17. A constant signal tuned to result in an average ToT of 15 ns is provided to all of the Padiwa channels. The recorded ToT distributions on all channels, as shown in Figure 3.20, are then fitted with a Gaussian function and the mean value of the fit is taken. The multiplicative calibration factors are determined by the division of the mean ToT value of each channel to the entire mean of all the channels on the corresponding module layer. The obtained calibration factors are given in Figure 3.21.

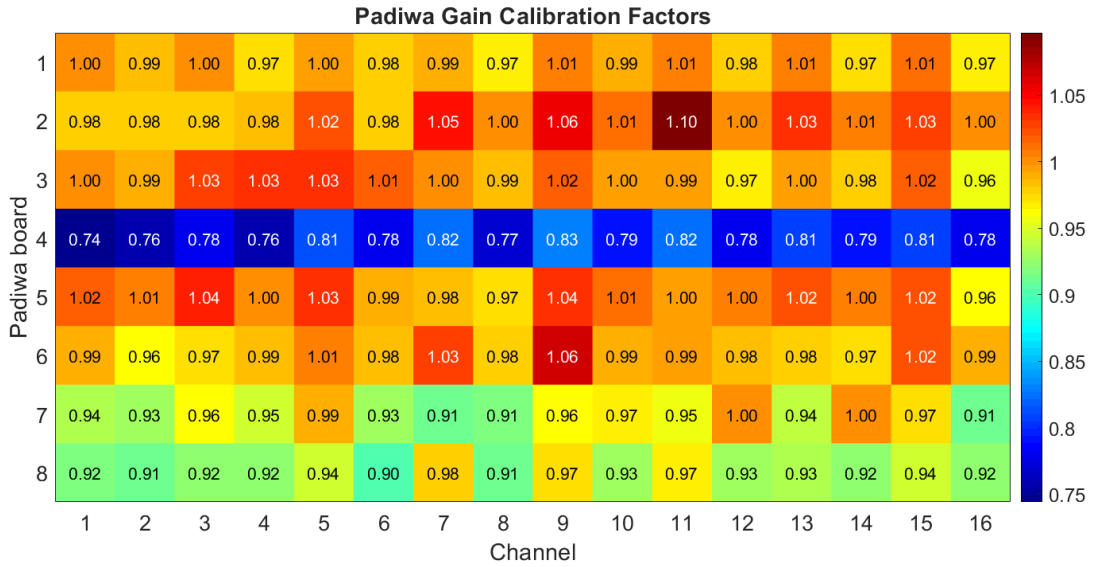


Figure 3.21: The obtained ToT calibration factors to alleviate the differences in amplification on different Padiwa channels.

By multiplying the measured ToT values with the determined calibration factors, it is thus possible to force all channels to have a peak mean at the same value. This correction is applied to the recorded ToT distribution and the resulting distribution is shown in Figure 3.22. It can be observed that the zigzag pattern in the Layer 2 is vanished after the correction as expected and the mean ToT distribution of all the channels are overlapping. With this, the ToT response of all the channels on the assembled readout electronics are calibrated. For signals with ToT values not close to  $\sim 15$  ns, this calibration is observed not to be accurate, but since the expected signals from MIPs is in this range this is satisfactory for the measurements with cosmic particles and pions from the conducted beam test. In addition to the variances in amplifiers on the Padiwas, another source of differences in the ToT response of channels in the fully assembled detector is the RadMap module itself. This also needs to be corrected. The procedure is presented in Section 3.3.2.

### 3 Development of a readout system for the RadMap telescope

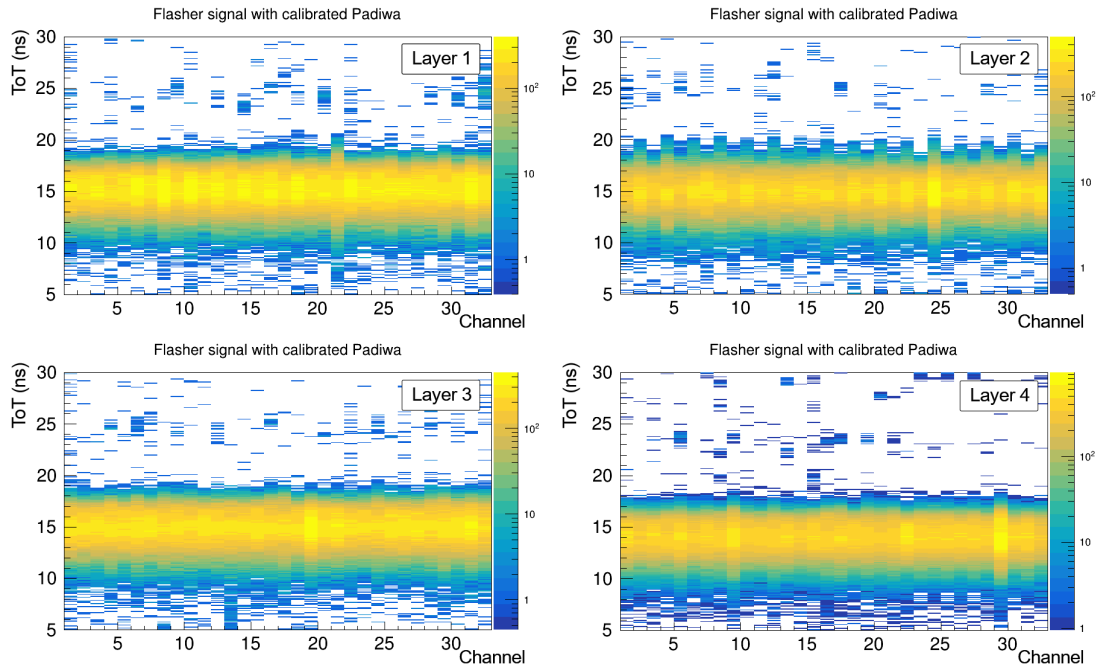


Figure 3.22: ToT distribution of signals recorded with Padiwas connected to the flasher setup corrected for the variances of amplification on different channels.

## 3.3 Commissioning with a beam test

### 3.3.1 The experiment

The 12 modules produced for the RadMap telescope project were tested and characterized in the large Ring Cyclotron complex at the Paul Scherrer Institute (PSI) in Switzerland. This opportunity was also used to test the developed particle tracker utilizing one of the spare RadMap modules with the ToT based readout system. A photo of the PSI Ring Cyclotron is shown in Figure 3.23. It can accelerate protons to 80% of the speed of light (equivalent to the kinetic energy of 590 MeV) and with a beam current of 2200  $\mu\text{A}$  it provides the most intense proton beam in the world [62, 63]. The cyclotron is operated with a frequency of 50.65 MHz with the protons reaching their terminal velocity on average in 186 revolutions [64]. Furthermore, beams composed of



Figure 3.23: The large PSI Ring Cyclotron. The turquoise structures are the eight sector-magnets and between them in dark grey the four acceleration cavities. *Photo: Markus Fischer/ PSI*

different particle species such as muons, pions and neutrons can be generated by colliding the initial proton beam with a fixed target and then refocusing the produced particle shower into a beam. Throughout the measurement campaign, two beam configurations containing pions or protons were used. The results presented in this thesis concern exclusively the data obtained with the pion beam as this approximates the intended use case of the assembled tracker detecting cosmic minimum ionizing particles. Whereas the proton runs were conducted mainly for the qualification and the characterization of the RadMap telescope.

The pion beam contains minimum ionizing pions with a momentum ( $p$ ) of 450 MeV/c. This corresponds to a kinetic energy ( $E_k$ ) of 331 MeV calculated with:

$$E_k = E - mc^2 = \sqrt{p^2c^2 + m^2c^4} - mc^2$$

The expected energy loss of pions crossing the entire thickness of 2 mm can be determined using the WebAtima tool [65], where the density of the fiber is taken as  $0.2064 \text{ g cm}^{-2}$  with a stopping power of  $\sim 1.8 \text{ MeV cm}^2 \text{ g}^{-1}$  [66]. The calculated total energy loss per fiber is  $\sim 0.4 \text{ MeV}$ . With this, it is expected that pions will penetrate the entire module and that signals should be registered on all layers.

Analysing the recorded data, firstly, the position of the beam spot on the module is determined. Figure 3.24 shows the position distribution of registered pion hits. It can be observed that the module was good aligned with the beam where the peak particle flux is recorded in the center region of the active area which covers  $\sim 64 \text{ mm} \times 64 \text{ mm}$ . The beam spot radius, taken as the Full-Width-at-Half-Maximum (FWHM) of the recorded particle distribution, is determined to be  $\sim 40 \text{ mm}$ .

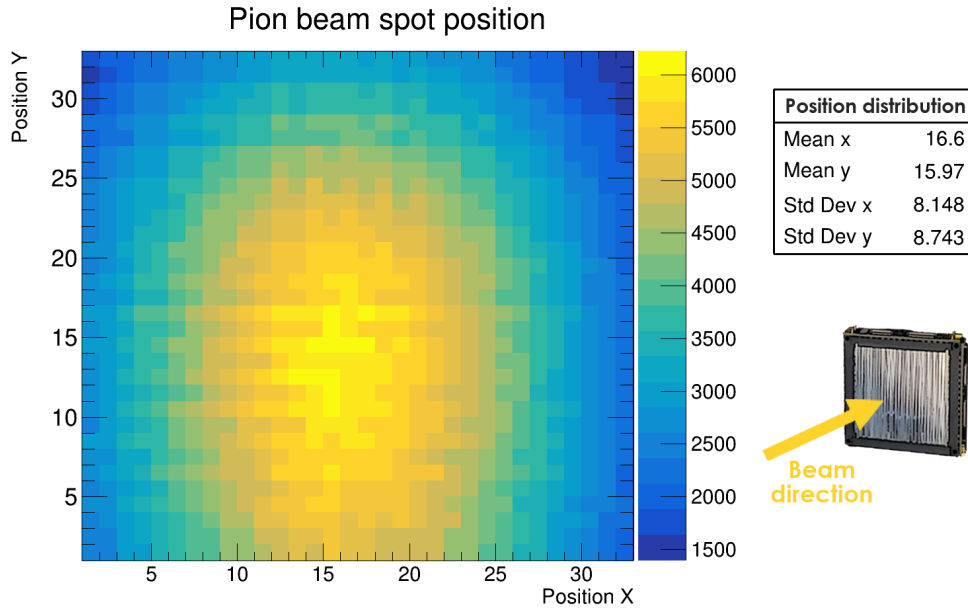


Figure 3.24: The beam spot measured with the tracker. The position on the axes are given in fibers.

Secondly, the time information of the recorded hits from the beam is analysed. In

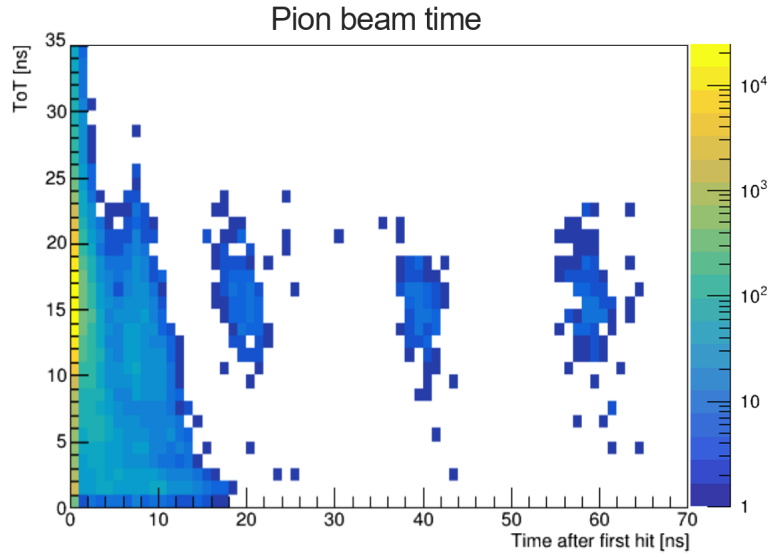


Figure 3.25: Hits recorded within CTS events plotted as a function of their time relative to the first hit in the event.

Figure 3.25 the timestamp of recorded hits relative to the first recorded hit within the corresponding CTS event is shown. It can be observed that within the CTS event time window multiple pion hits (recognized by their ToT value lying within the range of 10 ns to 20 ns) are recorded with a periodicity of  $\sim 20$  ns. This value matches the flattop cavity frequency of the accelerator, however, the beam is typically only extracted after 192 revolutions [64]. This would mean that the time difference between two pions should typically be in the order of  $\sim 4 \mu\text{s}$ . The observed higher particle rate is explained by runaway protons being extracted from the accelerator behind or ahead of the beam schedule.

### 3.3.2 Module gain calibration

The ToT distribution of the signals from all of the acquired signals is given in Figure 3.26. The presented data is with the Padiwa gain calibration described in Section 3.2.2 applied. One of the Padiwas reading out layer 2 having higher amplification results in alternating channels having different distribution widths even with the Padiwa gain calibration applied, which only corrects the mean position of the distribution. The signal peaks at a ToT value of  $\sim 15$  ns are associated with pion signals. However, it is possible to observe that the peak position of all the channels does not perfectly overlap. No variation is expected in the interaction of pions with different parts of the detector. As such, this discrepancy is introduced by the module hardware. Specifically, variations in the optical coupling of the fibers with SiPMs and the variations in the gain of the used SiPMs lead to the observed behaviour. The interface between the scintillating fibers and the corresponding SiPMs is achieved by optical glue, which is applied manually, is expected to be the main source. The correction of these module gain variations is crucial for the capability of the tracker to accurately represent the energy loss of the

### 3 Development of a readout system for the RadMap telescope

recorded particles.

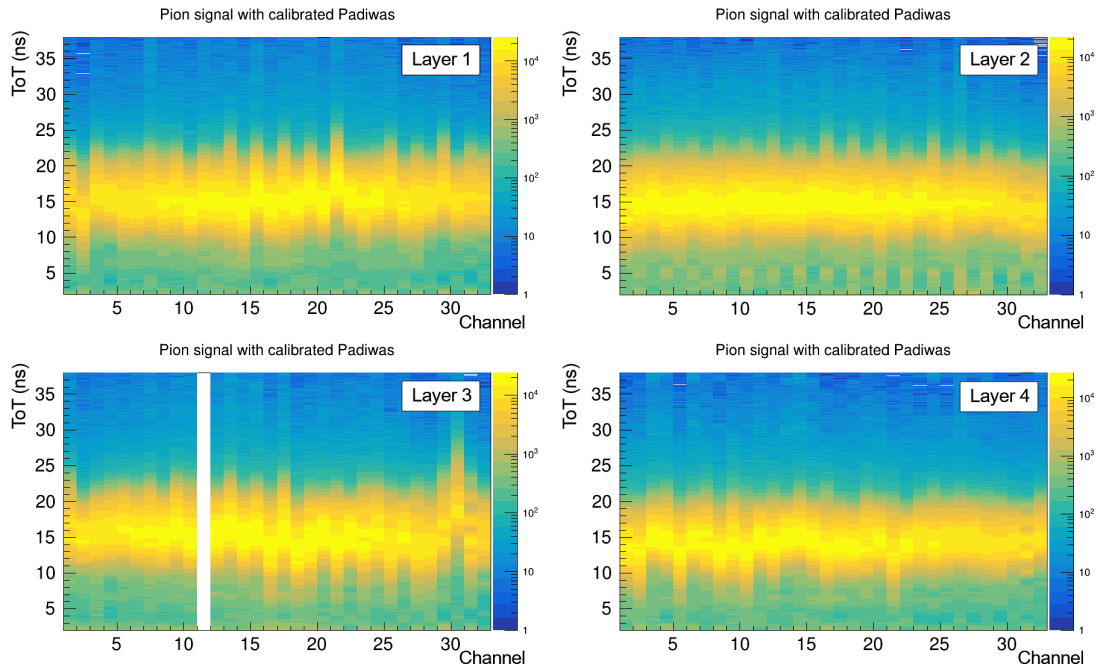


Figure 3.26: ToT distribution of signals recorded with the developed tracker system measuring pion beam at the PSI. The Padiwa gain calibration from Section 3.2.2 is applied. The empty Channel 11 on Layer 3 corresponds to a dead SiPM on the module.

The procedure of fitting the distributions with Gaussian function and calculating multiplicative calibration factors introduced in Section 3.2.2 is conducted with the recorded pion data. This includes not only the detector configuration shown in Figure 3.13 where the top four layers of the module are read out but by plugging the Padiwas to the other positions of the adapter PCBs, the bottom four layers of the module were also characterized. The resulting calibration factors describing the module gain variances are given in Figure 3.27.

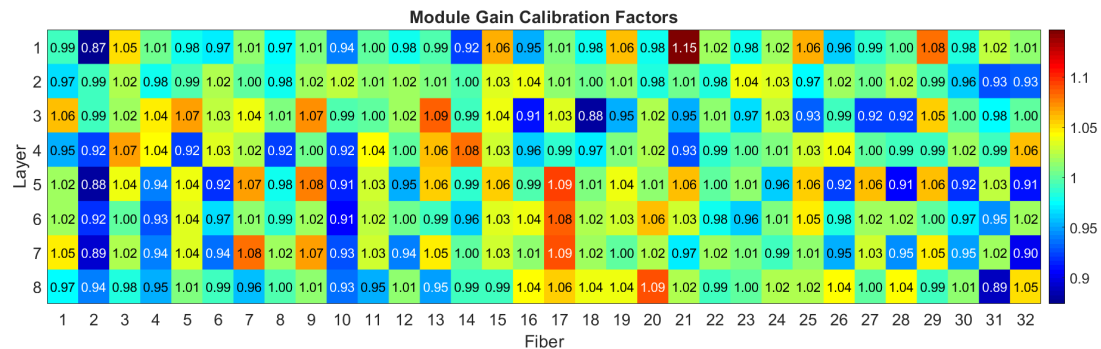


Figure 3.27: The obtained calibration factors to alleviate the differences between channels on the used RadMap module.

### 3 Development of a readout system for the RadMap telescope

By applying the obtained calibration to the recorded signals in post-processing the ToT distribution shown in Figure 3.28 is obtained. Here it is possible to observe that all channels have overlapping peak positions. With this, the detector is fully calibrated.

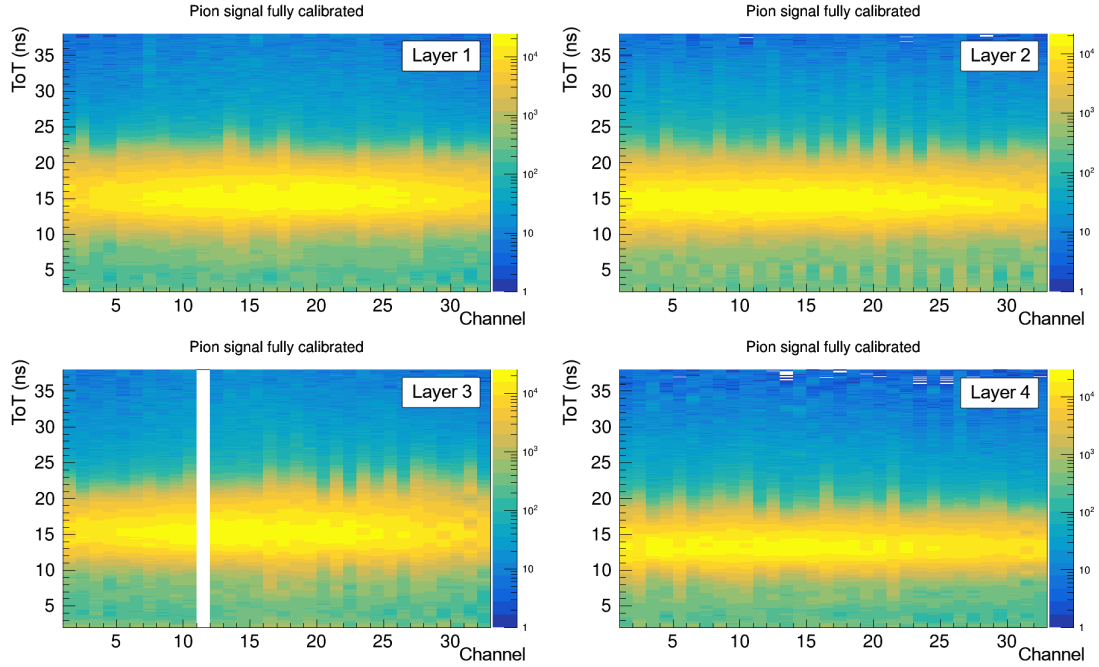


Figure 3.28: Fully calibrated ToT distribution of pion signals measured with the developed setup.

#### 3.3.3 Particle tracking

The determination of the trajectory of the particles in space using the recorded hits on various channels is required for the operation of the detector as a particle tracker. However, this is not a trivial operation and requires multiple steps of processing. Firstly, it is crucial to identify and filter out the fake hits introduced by the EMI noise and other sources described in Section 3.2.2. For this, a cut on ToT value is applied, where signals with a ToT smaller than 5 ns are not considered in the following steps. Furthermore, although the beam direction is perpendicular to the layer of the module, it is not guaranteed that a single particle will lead to only one signal on each layer. Pions going through two fibers as visualised in Figure 3.29 can lead to hits on two adjacent fibers. Also, and more prominently, the real signal from pions can be accompanied with fake hits on neighbouring channels introduced by crosstalk.

Multiple hits on layers increase the complexity of track reconstruction substantially. For this reason, a simple clustering is introduced, where signals on neighbouring channels are grouped into clusters if they occur within a 10 ns time window. An example event reconstructed into clusters is displayed in Figure 3.30 with a manually fitted track indicating how the associated track reconstruction might appear. It is important to note that a complete tracking framework is currently under construction.

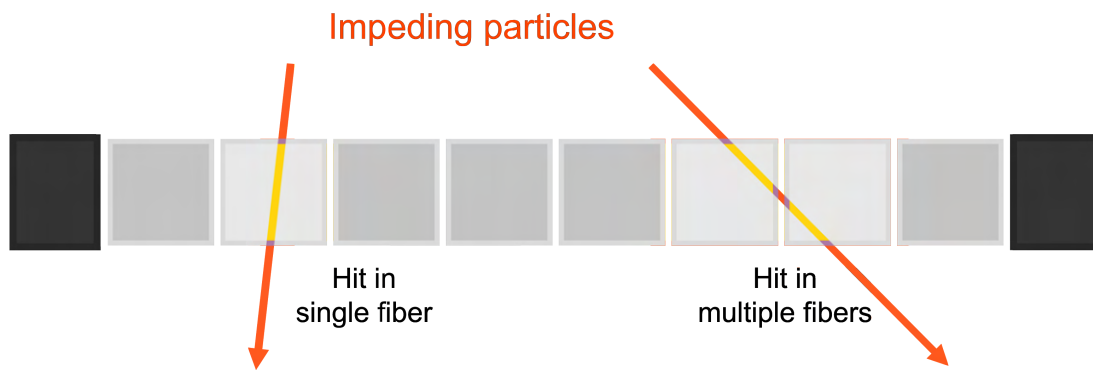


Figure 3.29: Sketch depicting two possible cases of particle trajectory. On the left, the more likely event where the particle crosses a single fiber on each layer. On the right, rare but possible events where a particle can hit two fibers on the same layer.

### 3.3.4 Detection efficiency calculations

Finally, the detection efficiency of the detector can be determined, given the assumption that pions cross all detector layers. For this, first, the efficiency of each layer is needed to be determined. The detection efficiency per layer is defined as the probability of registering a signal when a particle crosses the layer. Without utilizing an additional calibrated detector that has a very high and well known detection efficiency it is not possible to declare when a particle enters the active area of the module. In the presented case, no such detector was available and it is necessary to conduct the calculation only with the information obtained from the module itself. As such, it is crucial to establish methods to distinguish between real hits and fake hits.

Hits are assumed real if the following criteria are met. Firstly, the ToT of the signal should be larger than 5 ns as it is shown that EMI induced fake hits lie mostly below this range. Second, all real signals from consequent layers should be registered within 4 ns. This range is larger than what is expected from a pion crossing the entire module, however time delays between different channels are shown to be in the order of few nanoseconds even with the time calibration described in Section 3.2.2 applied. Finally, signals on vertical layers (1&3) and horizontal layers (2&4) should be registered within  $\pm 1$  fiber, as the incident angle of pions from the beam is very close to 90 degrees. Events, where at least 3 layers fulfill these requirements, are ultimately taken as real events. Considering all the mentioned definitions, the layer detection efficiency is defined as the probability of a layer registering a hit if and only if the other 3 layer also have real hits.

This is calculated by counting all events where a real hit is missing in a layer and subtracting this from the number of events with real hits on all layers. With the pion data the single layer detection efficiencies of all layers are determined. In addition, the detection efficiency of the full detector is defined as the probability that a particle will register hits on four layers, which is the minimum required for track reconstruction. Therefore, in the configuration where only half the module is readout as described

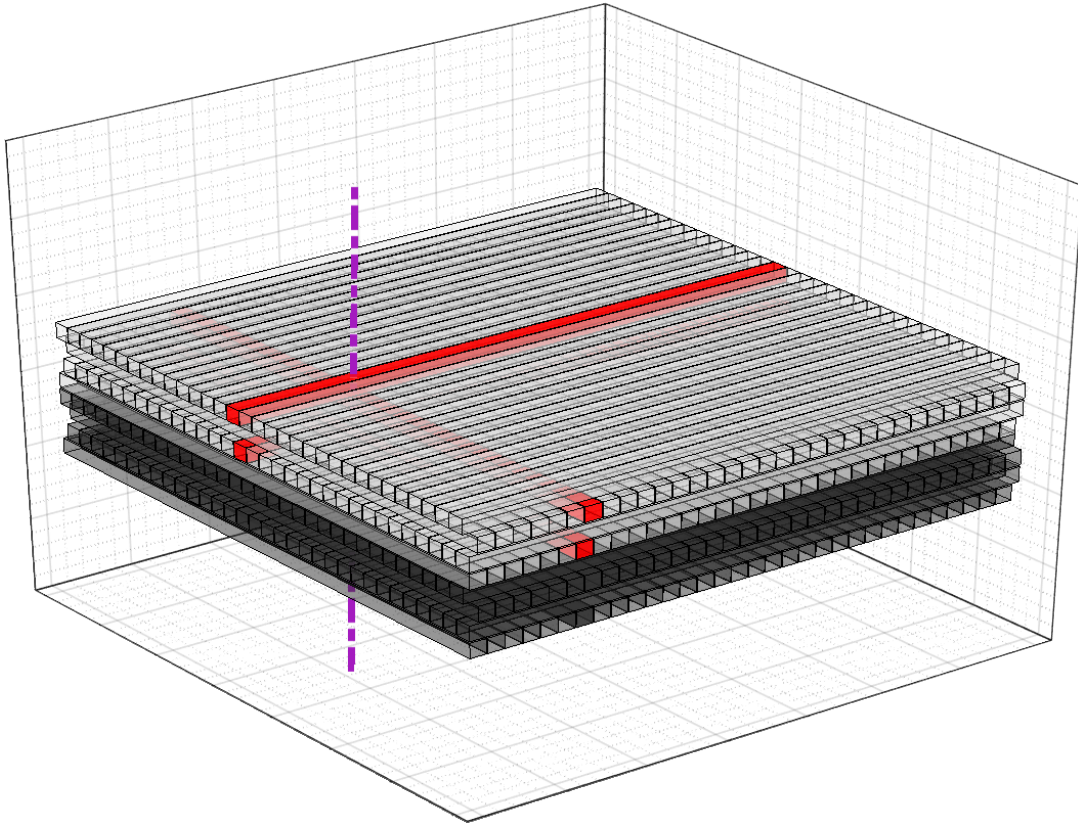


Figure 3.30: An example event display of the module. The red fibers indicate constructed cluster positions. Dark fibers are not read out. A manually fitted track using the cluster positions is also shown as indication of the corresponding pion trajectory.

|                 | Detection efficiency |
|-----------------|----------------------|
| Layer 1         | 90%                  |
| Layer 2         | 90%                  |
| Layer 3         | 87%                  |
| Layer 4         | 90%                  |
| First 4 Layers  | 64%                  |
| Layer 5         | 91%                  |
| Layer 6         | 92%                  |
| Layer 7         | 91%                  |
| Layer 8         | 92%                  |
| Second 4 Layers | 70%                  |

Table 3.1: The determined pion detection efficiencies of individual layers and the module with only half of layers read out.

### *3 Development of a readout system for the RadMap telescope*

here, this is calculated as the multiplication of all four single layer efficiencies. The determined values are shown in Table 3.1. Looking at the resulting numbers, it is possible to recognize that Layer 3 has less efficiency compared to the rest. This is explained by the dead channel, see Figure 3.26, reducing the active area of the layer by  $\sim 3\%$  which is consistent with the efficiency reduction. Still, the average layer efficiency lying roughly at 90% is lower than what would be expected when only the inactive cladding layer, making up only 2% of each fiber, is considered. This is partially explained by air gaps between the fibers which can be barely observed in Figure 3.12. Additional possible sources of inefficiencies are being investigated.

The detection efficiency of the investigated module determined with the described Padiwa+TRB3 readout electronics is in agreement with the performance observed using the ADC readout system developed for the RadMap telescope. The dedicated readout system was further used to characterize all twelve produced modules and the four best performing modules in terms of efficiency are selected to be used in the final flight setup. The modules containing dead channels, such as the one shown in this thesis are reserved as spares. Therefore, the discussed and an additional spare module will be used in further tests with ToT based readout systems operated specifically as a trigger for other detectors.

## 4 Conclusion and outlook

In the course of the work presented in this thesis, various types of particle detector technologies are operated and studied. These include firstly, Gas Electron Multipliers (GEM), a Micro-Pattern-Gas-Detector which is commonly utilized in major particle physics experiments, and secondly Silicon Photomultipliers (SiPM), which are being utilized in the RadMap telescope project, a compact radiation monitor system planned to be deployed to the ISS.

In the conducted studies, GEMs are investigated in terms of their stability against the formation of discharges. For this, several GEM and THGEM foils, which are produced at CERN, with various cladding materials have been tested and compared. In addition to their overall discharge stability also the light emitted by discharges in these detectors are analysed using optical spectroscopy techniques. The observed emission lines in the discharge spectra include those which are associated with the GEM electrode material. This supports the hypothesis of material evaporation during the breakdown events. However, in light from foils with THGEM geometry, no electrode material emission lines are detected. This suggests much less or no material evaporation during the THGEM discharge process, which can be explained by the higher faster dissipation of the discharge heat with the thicker conductor layers in THGEMs. Still, in terms of the overall stability against secondary discharges, it is observed that THGEMs don't show increased robustness in comparison to the used GEMs. As such, it can be concluded that the quantity of material evaporation or the maximum temperatures reached during primary discharges are not driving factors in secondary discharge formation. With this, it is demonstrated that optical spectroscopy can be a capable tool for studying discharges in MPGDs.

Additionally, a strong variance in secondary discharge stability is observed between THGEMs with different materials. The observed hierarchy between the materials doesn't follow any of the material properties expected to be relevant for discharge formation (e.g. conductivity, work function, melting temperature). As such, the secondary discharge phenomenon remains not fully understood. Even so, the observed material dependence of secondary discharge stability is likely to play a role in solving the secondary discharge formation puzzle. Furthermore, among the different THGEMs used in the studies, the one cladded with molybdenum is shown to be far superior in terms of stability against secondary discharges. This suggests molybdenum as a great candidate for the conductive material of choice for future GEM detectors. To this point, it is crucial to confirm this observation with further samples, including single and multi-hole GEM and THGEM structures.

Furthermore, the development of a ToT based readout system is conducted and its operation in particle tracking applications is successfully demonstrated. For this, a spare Active Detection Unit module produced for the RadMap telescope project is used. The

module incorporates 256 scintillating fibers coupled to silicon photomultipliers, with which the scintillation light induced by particles entering the fibers can be converted to electrical signals. The readout of generated analog signals is achieved with 128 channel ToT based readout system featuring Padiwa+TRB3 readout electronics. Before operation with the module, the readout system is calibrated in terms of the time information and the ToT value registered for signals on different channels. Moreover, the expected noise and crosstalk induced fake hit rates are investigated for various operation conditions. The module and the readout system are then assembled and operation procedures are established. Subsequently the assembled detector is tested using a pion beam in PSI in Switzerland. In the recorded data, pion induced signals are successfully identified, showing that the utilized readout system can reliably register signals from pions. Herewith, the detection efficiency of the used module is determined and found to be in agreement with the efficiency observed using the dedicated readout electronics developed for the RadMap telescope. Finally, the development of framework for the reconstruction of tracks from the recorded signals is initiated. In conclusion, the assembled detector can be dependably operated for tracking MIPs.

### 4.1 ToT based trigger for THGEM photon detector

The study of discharge stability of (TH)GEMs and the operation of the assembled particle tracking system are tied together in an ongoing project of developing THGEM based photon detectors. GEM based detectors, like other gaseous ionization detectors are not traditionally capable of detecting single VUV photons. This is due to the fact that the energy of these photons is not high enough to ionize any or enough number of gas atoms (e.g. ionization energy for Argon = 15.76 eV [37]) in the detector volume, which is necessary for generating strong signals to be reliably measured. And yet, by utilizing a photocathode material with a lower work function such as Cesium Iodide ( $W_{CsI} = 2.1$  eV [67]), the signal yield can be greatly increased. With this, it is planned to manufacture coated THGEMs which would act not only as a photocathode but also an amplification structure. Using this, it is possible to construct large area photon detectors much more cost effectively compared to for example using multiple photomultiplier tubes.

In reality however, this approach accompanies some critical hurdles which are being currently tackled. First of all, commonly used photocathode coating materials such as CsI are very fragile and cannot be operated for long time periods in a GEM detector due to the used gas mixtures and ion bombardment without significant degradation. Furthermore, since the amount of electrons emitted even when a photocathode material is used is quite low, the performance of the amplification stage is critical. As such, the THGEM is required to be operated in a way which maximizes the fraction of electrons which are not captured by the bottom THGEM electrode after the avalanche process inside the hole. However, this electron extraction is limited by the onset of secondary discharges with high induction fields below the THGEM. For this reason, the potential discovery of molybdenum as an electrode material which is much more stable against secondary discharges (discussed in Section 2.3.2) is very exciting.

Besides, for the qualification of such a prototype THGEM based photon detector, an external trigger system is required. It should be capable of reliably detecting particles and tracking them. Only with this, it is possible to determine the efficiency performance of the photo-THGEM, as otherwise it won't be known how many particles entered the active area of the detector. Such a trigger system is currently being developed by utilizing two spare modules produced for the RadMap telescope project (introduced in Section 3). The modules will be readout with a DiRICH module, which is based on the same design and ToT based processing as the Padiwa front-end cards (introduced in Section 3.2). The DiRICH supports 356 signal channels enabling the readout of one and a half modules. For the initial commissioning of the photo-THGEM prototypes it is foreseen to place the two modules one on top and one on bottom of the detector to conduct measurements with cosmic muons.

Finally, the results obtained with THGEMs incorporating different materials presented in this thesis have also been submitted to a journal (Nuclear Instruments and Methods in Physics Research Section A: Accelerators, Spectrometers, Detectors and Associated Equipment) and have been accepted to be published.

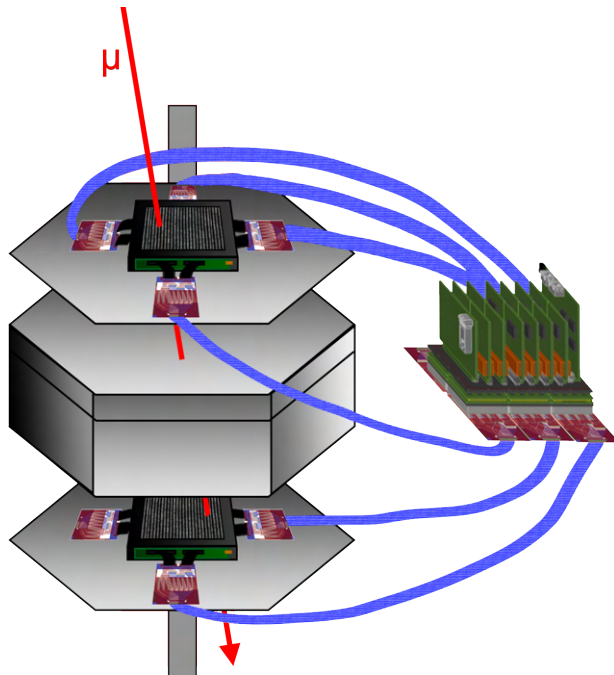


Figure 4.1: Setup where two RadMap modules are used with a DiRICH based readout as trigger for a THGEM photon detector. Utilizing the quasi-omnidirectional tracking capabilities of the modules enables a trigger logic beyond simple coincidence conditions of single channel triggers. With this, operation with cosmic particles is possible, which have a wide range of incidence angles.

## Acknowledgments

Throughout this thesis, I have received a great deal of support and assistance. First of all, I would like to thank Prof. Laura Fabbietti for her guidance and support throughout the conducted projects. An acknowledgement is never complete without thanking Dr. Piotr Gasik for his never-ending supply of amazing support and guidance. I would like to thank Prof. Dr. Reinhard Kienberger for his kind support. I would like to thank Thomas Klemenz for all the great discussions, comments and of course for the work he put into making all this possible. Similarly, I would like to thank Tobias Waldmann for his continued assistance in the lab. It goes without saying that I would also like to thank all remaining members of the GEMcrew. I would like to thank Dr. Michael Böhmer for his support and patience, Dr. Roman Gernhäuser and Stephan Königstorfer for their assistance. My sincere appreciation goes to the Dense and Strange Hadronic Matter group. And finally, I would like to give my deepest thanks to my family, friends and girlfriend for their help and companionship.

# List of Figures

|      |  |    |
|------|--|----|
| 2.1  | <i>(left)</i> Picture of a GEM foil section captured with an electron microscope. The conical GEM holes with a diameter of 70 $\mu\text{m}$ and the individual layers making up the 50 $\mu\text{m}$ thick foil can be recognized. <i>(right)</i> Sketch depicting the cross-section of GEM foil holes. The electric field enhancement inside the hole due to the geometry of the structure is also shown. [3] . . . . . | 3  |
| 2.2  | Side-by-side comparison between standard GEM and THGEM foil cross-sections. . . . .  | 4  |
| 2.3  | <i>(left)</i> Scheme of a GEM detector portraying a primary discharge that occurs inside a GEM hole, followed by a secondary discharge developed in the gap between the GEM and the readout electrode. <i>(right)</i> Electrical signals induced by different types of discharges on the readout plane. .  | 6  |
| 2.4  | Sketch depicting the evolution of a streamer discharge. A conductive plasma channel between the top and bottom GEM electrodes is formed leading to a breakdown. [17] . . . . .   | 6  |
| 2.5  | The used GEM and single-hole THGEMs. . . . .   | 9  |
| 2.6  | Microscope images of the THGEM holes seen from the induction side. .   | 11 |
| 2.7  | Schematic picture of the experimental setup and the detector geometry.   | 12 |
| 2.8  | Deuterium lamp setup used to measure the absolute intensity calibration.   | 14 |
| 2.9  | The measured and manufacturer provided spectra of the used calibrated Deuterium lamp. The observed difference is due to the intensity response of the various components in the setup. . . . .   | 15 |
| 2.10 | Discharge light spectra of Aluminium THGEM discharges measured in Ar-CO <sub>2</sub> (90-10) mixture and pure argon. The blue spectrum is scaled down by a factor of 1/3. See text for details. . . . .  | 16 |
| 2.11 | Example of the background removal procedure for a copper GEM discharge spectrum. The continuous background of the original spectrum (black) is fitted (blue) and subtracted. The red plot shows the resulting spectrum after background subtraction. See text for details. . . . .   | 17 |
| 2.12 | Primary discharge light spectra of a copper THGEM operated with pure argon and pure neon. The emission lines associated with the noble gases are designated. . . . .   | 18 |
| 2.13 | Emission spectra of primary spark discharges in copper GEM detector in Ar-CO <sub>2</sub> (90-10) mixture. Gas components and copper emission lines can be identified, the latter pointing to the vaporization of GEM foil material during a discharge. . . . .  | 19 |
| 2.14 | Comparison of emission spectra of primary spark discharges in copper and aluminium standard GEM foils. The emission peaks of the foil materials can be easily distinguished. . . . .   | 20 |

*List of Figures*

|      |   |    |
|------|---|----|
| 2.15 | Comparison between GEM and single-hole THGEM primary spark discharge emission spectra obtained with copper (left) and aluminium (right) cladding. . . . .   | 21 |
| 2.16 | Emission spectra from primary spark discharges measured with single-hole THGEM foils with different cladding materials. No emission lines associated with the THGEM materials can be identified. All spectra share peaks attributed to the gas mixture. . . . .   | 22 |
| 2.17 | Comparison of emission spectra between events with only a primary spark discharge and events where both primary and secondary discharges are recorded, measured with the tungsten THGEM. Except for the variance in overall intensity, the shape and the peak structure of the spectra are identical. . . . . | 23 |
| 2.18 | Secondary discharge probability as a function of the induction field measured with single-hole THGEMs with different coating materials. Field values are normalised to the ambient pressure of $\sim 960$ mbar measured for each data sample. . . . .   | 25 |
| 2.19 | Average time delay between primary and secondary discharges as a function of normalized induction field ( <i>top</i> ) and secondary discharge probability ( <i>bottom</i> ). Error bars indicate the Standard deviation of the mean. The copper GEM points taken as reference from [24]. . . . .             | 29 |
| 3.1  | Rendering of a fully assembled RadMap telescope [2]. . . . .  | 31 |
| 3.2  | The RadMap module used in the studies. . . . .  | 31 |
| 3.3  | Photograph of a fiber bunch before being installed into the modules. . .  | 32 |
| 3.4  | Representation of the fiber layout geometry . . . . .   | 32 |
| 3.5  | ( <i>left</i> ) Sketch depicting the cross section of the used scintillating plastic fibers. ( <i>right</i> ) Representation of the total reflection process utilized in transporting the scintillation light towards the readout. . . . .  | 33 |
| 3.6  | ( <i>top</i> ) Sketch depicting a cross section of a SiPM consisting of an array of microcells. Each microcell acts as a micro APD operated in Geiger-Mode and are connected to one another. ( <i>bottom</i> ) Photo of the SiPM configuration used in the RadMap modules. . . . .                            | 34 |
| 3.7  | The raw signal output from a single SiPM operated at different applied over-voltages. In all cases the SiPM is illuminated with a very faint constant light source from the LED flasher (ats4=75 with filter). . . . .  | 35 |
| 3.8  | The amplitude of the raw signal output from a single SiPM illuminated with a LED flasher as a function of the intensity setting of the flasher. The saturation curves for different applied SiPM voltages can be observed. . . . .  | 35 |
| 3.9  | ( <i>left</i> ) The Padiwa front end card responsible of converting the input signals from the SiPMs to time signals. ( <i>right</i> ) The TRB3 system housing the Time-to-Digital converters and the Central-Trigger-System for operating all the connected Padiwas. . . . .                                 | 37 |
| 3.10 | Adapter board between the RadMap module and the Padiwa front-end cards. . . . .   | 38 |

*List of Figures*

|      |   |    |
|------|---|----|
| 3.11 | Schematic depicting the filtering applied to the signals. The raw signal from the SiPM ( <i>left</i> ) is shaped on the adapter board with the given filter design. The output signal has a overshoot following the initial peak, which ensures that the signal will promptly go under threshold also with added noise. . . . .                                 | 38 |
| 3.12 | The RadMap module connected to four Padiwas via the produced custom adapter board. In the shown configuration, one of the four Ketek boards (64 channels, every second fiber in horizontal direction) on the module can be fully read out. . . . .  | 39 |
| 3.13 | The setup used in the test beam. The RadMap module with the scintillating fibers can be seen in the middle. Around it, two Padiwa cards are mounted on each of the four adapter boards. The detector was housed in a light tight box during operation. . . . .  | 40 |
| 3.14 | The noise recorded on one of the signal channels from the SiPM in dark conditions with an oscilloscope. With the Padiwa readout system connected, the observed noise is expected to be significantly higher due to the amplifiers with a gain of factor 10. . . . .   | 41 |
| 3.15 | How the oscillations of the signal lead to multiple hits with varying magnitudes when measured with the ToT method. . . . .   | 42 |
| 3.16 | The distribution of recorded proton hits on Layer 1 of the module plotted as a function of the measured ToT and the relative position to the first hit in the same event. . . . .   | 43 |
| 3.17 | Sketch depicting the setup for measuring the relative time delays between channels for time calibration. . . . .  | 44 |
| 3.18 | The difference in measured hit timestamp between different channels when a signal is sent simultaneously to all. Due to the different propagation times for all channels inside the FPGAs on the TRB3, different channels have different delays. The same delay pattern can be recognized in all TDC registers which have the same FPGA configurations. . . . . | 45 |
| 3.19 | Comparing the obtained time calibration values using the pulser setup with the time differences observed in the beam time in a configuration where pions go through all the fibers in a single layer. . . . .   | 46 |
| 3.20 | The ToT distribution of signals recorded with Padiwas connected to a single SiPM flashed with an LED light source. . . . .  | 47 |
| 3.21 | The obtained ToT calibration factors to alleviate the differences in amplification on different Padiwa channels. . . . .  | 48 |
| 3.22 | ToT distribution of signals recorded with Padiwas connected to the flasher setup corrected for the variances of amplification on different channels. . . . .  | 49 |
| 3.23 | The large PSI Ring Cyclotron. The turquoise structures are the eight sector-magnets and between them in dark grey the four acceleration cavities. <i>Photo: Markus Fischer/ PSI</i> . . . . .   | 49 |
| 3.24 | The beam spot measured with the tracker. The position on the axes are given in fibers. . . . .  | 50 |

*List of Figures*

|      |  |    |
|------|--|----|
| 3.25 | Hits recorded within CTS events plotted as a function of their time relative to the first hit in the event. . . . .  | 51 |
| 3.26 | ToT distribution of signals recorded with the developed tracker system measuring pion beam at the PSI. The Padiwa gain calibration from Section 3.2.2 is applied. The empty Channel 11 on Layer 3 corresponds to a dead SiPM on the module. . . . .  | 52 |
| 3.27 | The obtained calibration factors to alleviate the differences between channels on the used RadMap module. . . . .  | 52 |
| 3.28 | Fully calibrated ToT distribution of pion signals measured with the developed setup. . . . .   | 53 |
| 3.29 | Sketch depicting two possible cases of particle trajectory. On the left, the more likely event where the particle crosses a single fiber on each layer. On the right, rare but possible events where a particle can hit two fibers on the same layer. . . . .  | 54 |
| 3.30 | An example event display of the module. The red fibers indicate constructed cluster positions. Dark fibers are not read out. A manually fitted track using the cluster positions is also shown as indication of the corresponding pion trajectory. . . . .   | 55 |
| 4.1  | Setup where two RadMap modules are used with a DiRICH based readout as trigger for a THGEM photon detector. Utilizing the quasi-omnidirectional tracking capabilities of the modules enables a trigger logic beyond simple coincidence conditions of single channel triggers. With this, operation with cosmic particles is possible, which have a wide range of incidence angles. . . . . | 59 |

## List of Tables

|     |   |    |
|-----|---|----|
| 2.1 | Properties of the coating materials employed in this study [31, 32]. . . .  | 10 |
| 2.2 | The operational limit for the used THGEM foils before the onset of primary discharges. . . . .                            | 24 |
| 3.1 | The determined pion detection efficiencies of individual layers and the module with only half of layers read out. . . . . | 55 |

## Bibliography

- [1] F. Sauli. “GEM: A new concept for electron amplification in gas detectors”. In: *NIM A* 386 (1997), p. 531. URL: [https://doi.org/10.1016/S0168-9002\(96\)01172-2](https://doi.org/10.1016/S0168-9002(96)01172-2).
- [2] M. J. Losekamm, S. Paul, T. Pöschl, and H. J. Zachrau. “The RadMap Telescope on the International Space Station”. In: *2021 IEEE Aerospace Conference (50100)*. IEEE. 2021, pp. 1–10.
- [3] F. Sauli. “The gas electron multiplier (GEM): Operating principles and applications”. In: *NIM A* 805 (2016), p. 2.
- [4] S. Bachmann, A. Bressan, M. Capeáns, M. Deutel, S. Kappler, B. Ketzer, A. Polouektov, L. Ropelewski, F. Sauli, E. Schulte, et al. “Discharge studies and prevention in the gas electron multiplier (GEM)”. In: *NIM A* 479 (2002), p. 294. URL: [https://doi.org/10.1016/S0168-9002\(01\)00931-7](https://doi.org/10.1016/S0168-9002(01)00931-7).
- [5] A. Amoroso, R. B. Ferroli, I. Balossino, M. Bertani, D. Bettoni, A. Bortone, A. Calcaterra, S. Cerioni, W. Cheng, G. Cibinetto, et al. “Time performance of a triple-GEM detector at high rate”. In: *Journal of Instrumentation* 15.06 (2020), P06013.
- [6] ALICE TPC Collaboration. “The upgrade of the ALICE TPC with GEMs and continuous readout”. In: *JINST* 16 (Mar. 2021), P03022. URL: <https://doi.org/10.1088/1748-0221/16/03/p03022>.
- [7] A. Colaleo, A. Safonov, A. Sharma, and M. Tytgat. *CMS Technical Design Report for the Muon Endcap GEM Upgrade*. Tech. rep. June 2015. URL: <https://cds.cern.ch/record/2021453>.
- [8] D. S. Renous, A. Roy, A. Breskin, and S. Bressler. “Gain stabilization in Micro Pattern Gaseous Detectors: methodology and results”. In: *Journal of Instrumentation* 12.09 (2017), P09036.
- [9] M. Alfonsi, G. Croci, S. D. Pinto, E. Rocco, L. Ropelewski, F. Sauli, R. Veenhof, and M. Villa. “Simulation of the dielectric charging-up effect in a GEM detector”. In: *Nuclear Instruments and Methods in Physics Research Section A: Accelerators, Spectrometers, Detectors and Associated Equipment* 671 (2012), pp. 6–9.
- [10] B. Azmoun, W. Anderson, D. Crary, J. Durham, T. Hemmick, J. Kamin, G. Karagiorgi, K. Kearney, G. Keeler, E. Kornacki, P. Lynch, R. Majka, M. Rumore, F. Simon, J. Sinsheimer, N. Smirnov, B. Surrow, and C. Woody. “A Study of Gain Stability and Charging Effects in GEM Foils”. In: *2006 IEEE Nuclear Science Symposium Conference Record*. Vol. 6. 2006, pp. 3847–3851. DOI: 10.1109/NSSMIC.2006.353830.

## Bibliography

- [11] M. Pitt, P. Correia, S. Bressler, A. Coimbra, D. S. Renous, C. Azevedo, J. Veloso, and A. Breskin. "Measurements of charging-up processes in THGEM-based particle detectors". In: *Journal of Instrumentation* 13.03 (2018), P03009.
- [12] P. Correia, M. Pitt, C. Azevedo, A. Breskin, S. Bressler, C. Oliveira, A. Silva, R. Veenhof, and J. Veloso. "Simulation of gain stability of THGEM gas-avalanche particle detectors". In: *Journal of Instrumentation* 13.01 (2018), P01015.
- [13] V. Tikhonov and R. Veenhof. "GEM simulation methods development". In: *Nuclear Instruments and Methods in Physics Research Section A: Accelerators, Spectrometers, Detectors and Associated Equipment* 478.1-2 (2002), pp. 452–459.
- [14] S. D. Pinto, M. Villa, M. Alfonsi, I. Brock, G. Croci, E. David, R. de Oliveira, L. Ropelewski, and M. van Stenis. "Progress on large area GEMs". In: *Journal of Instrumentation* 4.12 (2009), P12009.
- [15] M. Villa, S. D. Pinto, M. Alfonsi, I. Brock, G. Croci, E. David, R. De Oliveira, L. Ropelewski, H. Taureg, and M. van Stenis. "Progress on large area GEMs". In: *Nuclear Instruments and Methods in Physics Research Section A: Accelerators, Spectrometers, Detectors and Associated Equipment* 628.1 (2011), pp. 182–186.
- [16] P. Fonte, V. Peskov, and F. Sauli. "VUV emission and breakdown in parallel-plate chambers". In: *Nuclear Instruments and Methods in Physics Research Section A: Accelerators, Spectrometers, Detectors and Associated Equipment* 310.1-2 (1991), pp. 140–145.
- [17] S. Franchino, D. G. Diaz, R. Hall-Wilton, H. Muller, E. Oliveri, D. Pfeiffer, F. Resnati, L. Ropelewski, M. Van Stenis, C. Strelti, P. Thuiner, and R. Veenhof. "Effects of high charge densities in multi-GEM detectors". In: *2015 IEEE Nuclear Science Symposium and Medical Imaging Conference (NSS/MIC)*. 2015, pp. 1–5. DOI: 10.1109/NSSMIC.2015.7581778.
- [18] P. Gasik, A. Mathis, L. Fabbietti, and J. Margutti. "Charge density as a driving factor of discharge formation in GEM-based detectors". In: *NIM A* 870 (2017), p. 116. URL: <https://doi.org/10.1016/j.nima.2017.07.042>.
- [19] A. Bressan, M. Hoch, P. Pagano, L. Ropelewski, F. Sauli, S. Biagi, A. Buzulutskov, M. Gruwe, G. De Lentdecker, D. Moermann, et al. "High rate behavior and discharge limits in micro-pattern detectors". In: *NIM A* 424 (1999), p. 321.
- [20] P. Fonte and V. Peskov. "On the physics and technology of gaseous particle detectors". In: *Plasma Sources Science and Technology* 19 (2010), p. 034021.
- [21] L. Lautner. *Influence of the charge density on discharges in THGEM-based detectors*. 2019. URL: [http://www.das.ktas.ph.tum.de/DasDocs/Public/Master\\_Theses/Master\\_Thesis\\_LukasLautner.pdf](http://www.das.ktas.ph.tum.de/DasDocs/Public/Master_Theses/Master_Thesis_LukasLautner.pdf).
- [22] L. Lautner, L. Fabbietti, P. Gasik, and T. Klemenz. "High voltage scheme optimization for secondary discharge mitigation in GEM-based detectors". In: *JINST* 14 (2019) P08024 (2019). URL: <https://doi.org/10.1088/1748-0221/14/08/P08024>.
- [23] V. Peskov and P. Fonte. "Research on discharges in micropattern and small gap gaseous detectors". In: *arXiv:0911.0463* (2009). URL: <https://arxiv.org/abs/0911.0463>.

## Bibliography

- [24] A. Deisting, C. Garabatos, P. Gasik, D. Baitinger, A. Berdnikova, M. Blidaru, A. Datz, F. Duffer, S. Hassan, T. Klemenz, et al. "Secondary discharge studies in single- and multi-GEM structures". In: *NIM A* 937 (2019), p. 168. URL: <https://doi.org/10.1016/j.nima.2019.05.057>.
- [25] A. Utrobicic, M. Kovacic, F. Erhardt, M. Jercic, N. Poljak, and M. Planinic. "Studies of the delayed discharge propagation in the Gas Electron Multiplier (GEM)". In: *NIM A* 940 (2019), p. 262. URL: <https://doi.org/10.1016/j.nima.2019.06.018>.
- [26] B. Ulukutlu and P. Gasik. "Studying secondary discharges with an optically read out GEM". In: *Journal of Physics: Conference Series*. Vol. 1498. 1. IOP Publishing. 2020, p. 012035.
- [27] R. Bouclier, W. Dominik, M. Hoch, J.-C. Labbé, G. Million, L. Ropelewski, F. Sauli, A. Sharma, and G. Manzin. "New observations with the gas electron multiplier (GEM)". In: *Nuclear Instruments and Methods in Physics Research Section A: Accelerators, Spectrometers, Detectors and Associated Equipment* 396.1-2 (1997), pp. 50–66.
- [28] T. Koike, S. Uno, T. Uchida, M. Sekimoto, T. Murakami, K. Miyama, M. Shoji, T. Fujiwara, E. Nakano, and J. Chiba. "A new gamma-ray detector with gold-plated gas electron multiplier". In: *NIM A* 648 (2011), p. 180. ISSN: 0168-9002. URL: <http://www.sciencedirect.com/science/article/pii/S016890021101076X>.
- [29] G. Song, M. Shao, L. Shang, Y. Zhou, Y. Lv, X. Wang, J. Liu, and Z. Zhang. "Production and properties of a charging-up "Free" THGEM with DLC coating". In: *NIM A* 966 (2020), p. 163868. ISSN: 0168-9002. URL: <http://www.sciencedirect.com/science/article/pii/S0168900220303685>.
- [30] B. Mindur, T. Fiutowski, S. Koperny, P. Wiącek, and W. Dąbrowski. "Investigation of Copper-Less Gas Electron Multiplier Detectors Responses to Soft X-rays". In: *Sensors* 20.10 (2020), p. 2784.
- [31] The Engineering ToolBox. "Material properties for gases, fluids and solids - densities, specific heats, viscosities and more". In: (2020). URL: [https://www.engineeringtoolbox.com/material-properties-t\\_24.html](https://www.engineeringtoolbox.com/material-properties-t_24.html).
- [32] G. N. Derry, M. E. Kern, and E. H. Worth. "Recommended values of clean metal surface work functions". In: *JVST A* (2015). DOI: <https://doi.org/10.1116/1.4934685>. URL: <https://avs.scitation.org/doi/pdf/10.1116/1.4934685>.
- [33] A. Utrobicic, M. Kovacic, F. Erhardt, N. Poljak, and M. Planinic. "A floating multi-channel picoammeter for micropattern gaseous detector current monitoring". In: *Nuclear Instruments and Methods in Physics Research Section A: Accelerators, Spectrometers, Detectors and Associated Equipment* 801 (2015), pp. 21–26.
- [34] Y. Assran and a. Sharma. "Transport Properties of operational gas mixtures used at LHC". In: (2011). URL: <https://arxiv.org/ftp/arxiv/papers/1110/1110.6761.pdf>.
- [35] Ocean Insight. *Ocean Insight Spectrometers*. URL: <https://www.oceaninsight.com/products/spectrometers/>.

## Bibliography

- [36] E. K. Plyler. "The Infrared Emission Spectra of CO<sub>2</sub> and H<sub>2</sub>O Molecules". In: *Science* 107 (1948), p. 48. URL: <https://science.sciencemag.org/content/107/2767/48>.
- [37] National Institute of Standards and Technology (NIST). *Basic Atomic Spectroscopic Data*. URL: [https://physics.nist.gov/PhysRefData/Handbook/element\\_name.htm](https://physics.nist.gov/PhysRefData/Handbook/element_name.htm).
- [38] C. M. Galloway, E. C. L. Ru, and P. G. Etchegoin. "An Iterative Algorithm for Background Removal in Spectroscopy by Wavelet Transforms". In: *Applied Spectroscopy* 63 (2009), p. 1370. URL: <https://journals.sagepub.com/doi/abs/10.1366/000370209790108905>.
- [39] J. Merlin. "Discharge and crosstalk mitigation for the GE21 system in CMS". In: *Presentation at the RD51 Collaboration Meeting 2020* (2020). URL: <https://indico.cern.ch/event/889369/contributions/4040763/>.
- [40] H. R. Griem. "Principles of Plasma Spectroscopy". In: *Cambridge Monographs on Plasma Physics*. Cambridge University Press, 1997, p. 54. URL: <https://doi.org/10.1017/CB09780511524578.005>.
- [41] J. Merlin. "Effect of discharges on GEM detectors - Single hole setup". In: *Presentation at the RD51 Collaboration Meeting 2018* (2018). URL: [https://indico.cern.ch/event/709670/contributions/3008626/attachments/1672294/2683230/JMERLIN\\_RD51ColMeeting\\_GEM\\_DischargeEffects\\_24052018.pdf](https://indico.cern.ch/event/709670/contributions/3008626/attachments/1672294/2683230/JMERLIN_RD51ColMeeting_GEM_DischargeEffects_24052018.pdf).
- [42] R. Honig and D. Kramer. "Vapor Pressure Data for the Solid and Liquid Elements". In: *RCA Review* 30 (1969), p. 285.
- [43] A. Deisting, C. Garabatos, and A. Szabo. "Ion mobility measurements in Ar-CO<sub>2</sub>, Ne-CO<sub>2</sub>, and Ne-CO<sub>2</sub>-N<sub>2</sub> mixtures, and the effect of water contents". In: *NIMA A* 904 (2018), pp. 1–8. ISSN: 0168-9002. DOI: <https://doi.org/10.1016/j.nima.2018.07.008>. URL: <https://www.sciencedirect.com/science/article/pii/S0168900218308313>.
- [44] L. Loeb. *Fundamental Processes of Electrical Discharge in Gases*. J. Wiley & Sons, Incorporated, 1939. ISBN: 9780598985774. URL: <https://books.google.de/books?id=m3LPAAAAAAAJ>.
- [45] L. B. Loeb and A. F. Kip. "Electrical Discharges in Air at Atmospheric Pressure The Nature of the Positive and Negative Point-to-Plane Coronas and the Mechanism of Spark Propagation". In: *Journal of Applied Physics* 10 (1939), p. 142. URL: <https://doi.org/10.1063/1.1707290>.
- [46] H. Raether. "Die Entwicklung der Elektronenlawine in den Funkenkanal". In: *Zeitschrift für Physik* 112 (July 1939), p. 464. ISSN: 0044-3328. URL: <https://doi.org/10.1007/BF01340229>.
- [47] J. M. Meek. "A Theory of Spark Discharge". In: *Phys. Rev.* 57 (8 Apr. 1940), p. 722. URL: <https://link.aps.org/doi/10.1103/PhysRev.57.722>.
- [48] J. S. Townsend. "The Conductivity produced in Gases by the Motion of Negatively-charged Ions". In: *Nature* 62 (Aug. 1900), p. 340. ISSN: 1476-4687. URL: <https://doi.org/10.1038/062340b0>.

## Bibliography

- [49] D. Xiao. *Gas Discharge and Gas Insulation*. Springer, Berlin, Heidelberg, 2016. URL: <https://link.springer.com/book/10.1007/978-3-662-48041-0#about>.
- [50] C. Walker, M. El-Gomati, A. Assa'd, and M. Zadrazil. "The secondary electron emission yield for 24 solid elements excited by primary electrons in the range 250–5000 eV: a theory/experiment comparison". In: *Scanning* 30 (2008), p. 365. URL: <https://onlinelibrary.wiley.com/doi/abs/10.1002/sca.20124>.
- [51] Kuraray. *Plastic scintillating fibers (PSF)*. 2021. URL: <https://www.kuraray.com/products/psf>.
- [52] W. R. Leo. *Techniques for nuclear and particle physics experiments: a how-to approach*. Springer Science & Business Media, 2012.
- [53] G. F. Knoll. *Radiation detection and measurement*. John Wiley & Sons, 2010.
- [54] KETEK. *Product data sheet for PM3325-WB-D0 SiPM*. 2020. URL: <https://www.ketek.net/wp-content/uploads/2018/12/KETEK-PM3325-WB-D0-Datasheet.pdf>.
- [55] A. Neiser, J. Adamczewski-Musch, M. Hoek, W. Koenig, G. Korcyl, S. Linev, L. Maier, J. Michel, M. Palka, M. Penschuck, et al. "TRB3: a 264 channel high precision TDC platform and its applications". In: *Journal of Instrumentation* 8.12 (2013), p. C12043.
- [56] M. Traxler. *TRB/DiRICH FEE Electronics and Readout System*. Aug. 2017. URL: <https://www.uni-giessen.de/fbz/fb07/fachgebiete/physik/institute/iipi/arbeitsgruppen/ag-dueren/aktuelles/DIRC2017/slides/dirctalks2017>.
- [57] A. Rost. *A flexible FPGA based QDC and TDC for the HADES and the CBM calorimeters*. 2016. URL: <http://jspc29.x-matter.uni-frankfurt.de/trbweb/uploads/2016TWEPPPadiwaAmps.pdf>.
- [58] T. Instruments. "LVDS application and data handbook". In: *Literature Number: SLLD009* (2002).
- [59] GSI. *DABC Homepage*. July 2021. URL: [https://www.gsi.de/en/work/research/experiment\\_electronics/data\\_processing/data\\_acquisition/dabc](https://www.gsi.de/en/work/research/experiment_electronics/data_processing/data_acquisition/dabc).
- [60] R. Brun and F. Rademakers. "ROOT—An object oriented data analysis framework". In: *Nuclear Instruments and Methods in Physics Research Section A: Accelerators, Spectrometers, Detectors and Associated Equipment* 389.1-2 (1997), pp. 81–86.
- [61] M. Boehmer. *Homepage of TUPHZEL Group*. 2021. URL: <https://www.ph.tum.de/research/groups/group/TUPHZEL/>.
- [62] W. Wagner, M. Seidel, E. Morenzoni, F. Groeschel, M. Wohlmuther, and M. Daum. "PSI status 2008—Developments at the 590 MeV proton accelerator facility". In: *Nuclear Instruments and Methods in Physics Research Section A: Accelerators, Spectrometers, Detectors and Associated Equipment* 600.1 (2009), pp. 5–7.
- [63] PSI. *The PSI Proton Accelerator*. 2021. URL: <https://www.psi.ch/en/media/the-psi-proton-accelerator>.

## Bibliography

- [64] M. Frey, J. Snuverink, C. Baumgarten, and A. Adelman. “Matching of turn pattern measurements for cyclotrons using multiobjective optimization”. In: *Physical Review Accelerators and Beams* 22.6 (2019), p. 064602.
- [65] Isotopea. 2021. URL: <https://www.isotopea.com/webatima>.
- [66] D. E. Groom and S. Klein. “Passage of particles through matter”. In: *The European Physical Journal C-Particles and Fields* 15.1 (2000), pp. 163–173.
- [67] S. Fairchild, T. Back, P. Murray, M. Cahay, and D. Shiffler. “Low work function CsI coatings for enhanced field emission properties”. In: *Journal of Vacuum Science & Technology A: Vacuum, Surfaces, and Films* 29.3 (2011), p. 031402.